

## Constructing and Forgetting Temporal Context in the Human Cerebral Cortex

### Highlights

- Distinct cortical responses when the same stimulus is preceded by different contexts
- Responses align as common input continues: sensory cortex, then higher-order cortex
- Cortical regions maintain a distributed and hierarchical representation of context
- Distributed cortical memory is gated and prior context can be flexibly forgotten

### Authors

Hsiang-Yun Sherry Chien,  
Christopher J. Honey

### Correspondence

chris.honey@jhu.edu

### In Brief

Chien and Honey measured how sequential information in a spoken narrative is integrated and separated in the human cerebral cortex. They observed a hierarchical representation of temporal context, distributed across the cortex. Computational modeling suggests the distributed context representation is flexibly updated or reset based on surprise.

# Constructing and Forgetting Temporal Context in the Human Cerebral Cortex

Hsiang-Yun Sherry Chien<sup>1</sup> and Christopher J. Honey<sup>1,2,\*</sup>

<sup>1</sup>Department of Psychological and Brain Sciences, Johns Hopkins University, Baltimore, MD 21218, USA

<sup>2</sup>Lead Contact

\*Correspondence: [chris.honey@jhu.edu](mailto:chris.honey@jhu.edu)

<https://doi.org/10.1016/j.neuron.2020.02.013>

## SUMMARY

How does information from seconds earlier affect neocortical responses to new input? We found that when two groups of participants heard the same sentence in a narrative, preceded by different contexts, the neural responses of each group were initially different but gradually fell into alignment. We observed a hierarchical gradient: sensory cortices aligned most quickly, followed by mid-level regions, while some higher-order cortical regions took more than 10 seconds to align. What computations explain this hierarchical temporal organization? Linear integration models predict that regions that are slower to integrate new information should also be slower to forget old information. However, we found that higher-order regions could rapidly forget prior context. The data from the cortical hierarchy were instead captured by a model in which each region maintains a temporal context representation that is nonlinearly integrated with input at each moment, and this integration is gated by local prediction error.

## INTRODUCTION

Events such as gestures, melodies, speech, and actions unfold over time, so we can only perceive and understand information in the present by integrating it with information from the past (Buonomano and Maass, 2009; Fuster, 1997; Kiebel et al., 2008). This process is complex because the world contains meaningful structure on scales ranging from milliseconds to minutes (Gibson et al., 1982; Poeppel, 2003; Zacks and Tversky, 2001); a series of phonemes makes up a word, a series of words forms a sentence, and a series of sentences expresses an idea. How is the human brain organized to integrate information across multiple timescales in parallel?

We and others have argued that the human brain employs a distributed and hierarchical architecture for integrating information over time (Baldassano et al., 2017; Fuster, 1997; Hasson et al., 2015; Honey et al., 2012; Lerner et al., 2011; Runyan et al., 2017). The architecture is distributed because almost all regions of the human cerebral cortex exhibit temporal context dependence in their responses. The architecture is hierarchical

because early sensory regions integrate over short timescales (milliseconds to seconds), while higher-order regions integrate information over longer timescales (seconds to minutes).

The timescale hierarchy is a highly reliable phenomenon with functional implications across the brain (Baldassano et al., 2017; Burt et al., 2018; Chaudhuri et al., 2015; Cocchi et al., 2016; Demirtaş et al., 2019; Watanabe et al., 2019), yet our models of the underlying information processing have remained phenomenological. What are the computations that integrate past and present information within the hierarchical networks of our brains? How is past and present information represented within each stage of processing and then passed on to higher stages? We set out to answer these questions using a combined empirical and modeling approach.

To investigate how information is integrated over time, prior studies have measured the “processing timescales” of different brain regions. Processing timescales were quantified by comparing a brain region’s response to a stimulus at time  $t$  across various contexts, where the stimulus properties at time  $(t - \tau)$  were altered. For example, Lerner et al. (2011) used functional magnetic resonance imaging (fMRI) to measure the neural responses to temporally manipulated versions of an auditory narrative (Figure 1A). They compared the responses during the original intact clip against the response during versions of the stimulus in which the ordering of words, sentences, or paragraphs was scrambled. The authors observed that early sensory regions exhibited similar responses to the intact and scrambled audio; these early regions were said to have a short processing timescale, because their responses at each moment were largely independent of prior context. Moving toward higher-order cortices, such as temporoparietal junction, precuneus, and lateral prefrontal cortex, Lerner et al. (2011) observed different responses to the intact and scrambled input. In these higher-order regions, the response at one moment could depend on stimulus properties from more than 30 s earlier (Figure 1B). Overall, higher stages of cortical processing were said to have longer processing timescales, because their responses at time  $t$  were affected by properties of the stimulus from many seconds earlier (Figure 1C).

In this study, we first developed computational models that could explain the key empirical phenomena from prior studies (e.g., Lerner et al., 2011). If we have measured the neural responses to temporally “intact” and “scrambled” versions of the stimulus, then we can quantify the similarity of responses to the same segment presented in the intact and scrambled order as the “intact-vs-scramble correlation” (Figure 1D). The

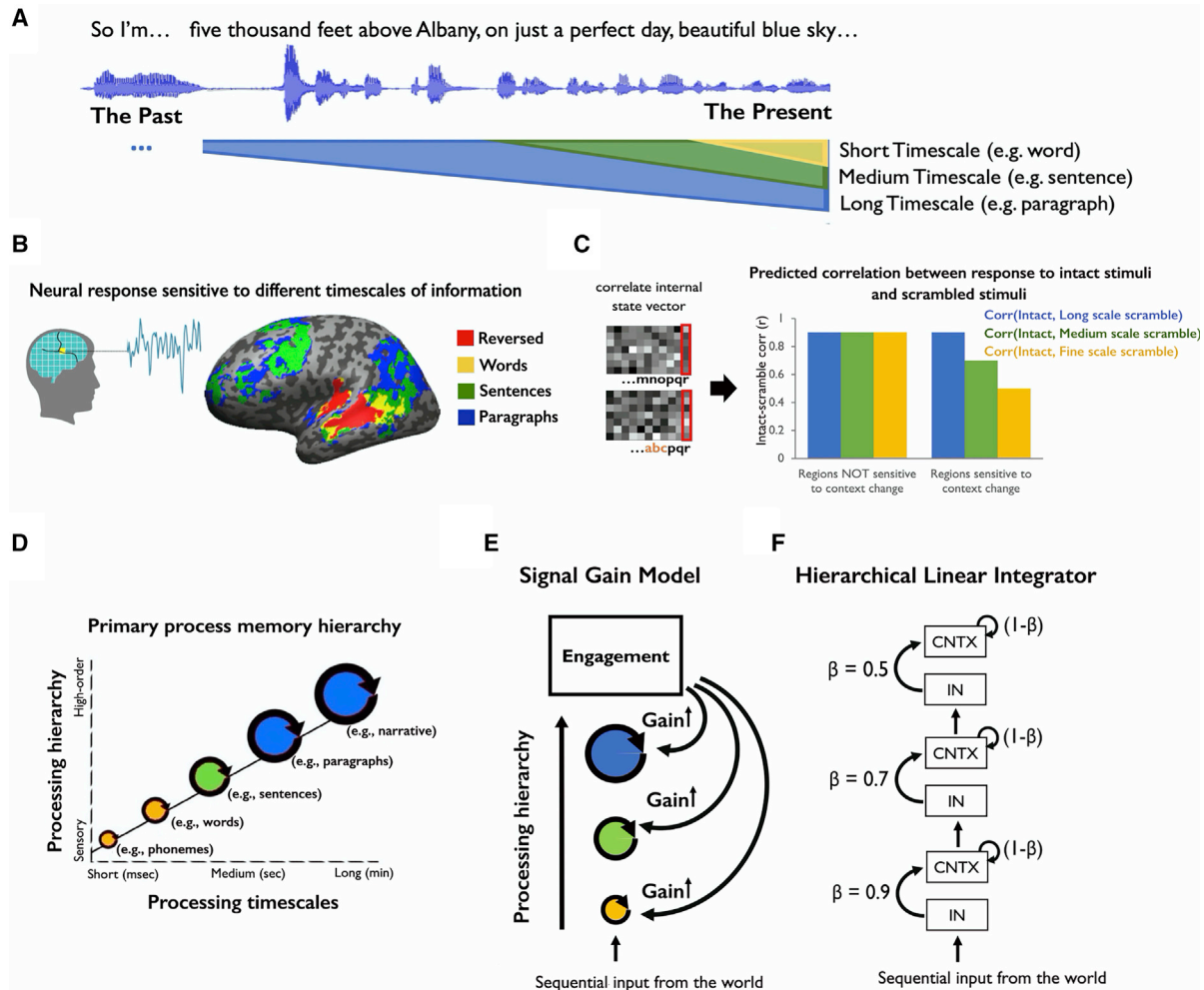


**Figure 1. Computational Models of Distributed and Hierarchical Process Memory**

(A) Schematic of experiment and results from Lerner et al. (2011). fMRI participants listened to an intact auditory narrative as well as versions scrambled at the scales of words, sentences, and paragraphs.

(B) Lower-level regions (e.g., auditory cortex) exhibited responses that were reliable across all stimuli, with little dependence on prior temporal context. By contrast, higher-level regions (e.g., precuneus) exhibited responses that depended at each moment on tens of seconds of prior context in the stimuli.

(C) Schematic of the “process memory hierarchy.” Lower-level regions (e.g., sensory regions) exhibit shorter integration timescales, integrating over entities such as phonemes and words. Higher-level regions (e.g., lateral and medial parietal regions) exhibited longer integration timescales, combining information on the scale of entire events (e.g., paragraphs of text).

(D) Schematic of predicted data when comparing the representations of brain regions sensitive to temporal context on different scales. The dependent variable is the “intract-scramble correlation,” quantifying the similarity of neural response to the same input in different contexts.

(E) Schematic of a signal gain model for explaining the pattern of brain responses shown in (D).

(F) Schematic of the hierarchical linear integrator (HLI) model.

two key phenomena of hierarchical context dependence are then as follows:

- (P1) lower processing stages are largely insensitive to temporal context (Figure 1D, left bars); and
- (P2) progressively higher processing stages are increasingly sensitive to temporal context extending further into the past (Figure 1D, right bars).

We found that P1 and P2 could be explained by a model that does not invoke explicit temporal integration (the “signal gain model”; Figure 1E) and also by a model that does employ tem-

poral integration (the “hierarchical linear integrator” [HLI] model; Figure 1F). To decide between these two models, we empirically tested a distinctive prediction of hierarchical integration models: when two people with distinct neural states are presented with a common input, their neural responses should gradually align over time as the common input continues, and this alignment should occur more slowly in higher-order regions.

Our empirical measurements revealed new evidence that cortical circuits hierarchically integrate input with prior context. We measured moment-by-moment changes in fMRI responses

as two groups of participants heard the same natural auditory speech segments preceded by different contexts. We found that the fMRI responses gradually aligned over time across the two groups, when each group heard the same input preceded by a different context. The responses aligned earliest in sensory regions but later and later in regions at consecutive stages of processing. This finding is consistent with the predictions of the HLI model but could not be explained by the signal gain model. Thus, the topography of these alignment patterns provides new evidence for a distributed and hierarchical representation of temporal context in the human brain.

If temporal integration is linear in the brain, then regions that are slower to integrate new information should also be slower to forget old information. But is this observed? To measure forgetting, we examined the rate at which fMRI states “separate” when two groups of participants begin with a common context, but are then exposed to distinct input. We found that, although higher-order regions aligned across contexts more gradually than sensory regions, they did not separate more gradually. This decoupling of alignment times and separation times rules out standard linear integrator models and seems to require a mechanism for flexibly varying how new and old information are combined.

Finally, to account for the decoupling between alignment times and separation times in cortical dynamics, we proposed a model of temporal integration, the hierarchical autoencoders in time (HAT) model. By combining non-linear integration and context gating mechanisms, HAT generated learning-dependent representations that account for the existing empirical phenomena (P1 and P2, above) while also exhibiting hierarchical alignment times and a distinct set of timescales for alignment and separation. In the HAT model, integration is flexible: at appropriate moments, such as the start of a new event, the model can generate a response that depends less on the prior context.

We conclude that each stage of cortical hierarchy maintains a temporal context representation, which is continually updated as a simplified combination of past and present information and which can also be reset following surprising input.

## RESULTS

We considered two computational models to account for the empirical phenomena P1 and P2: a model based on engagement with the stimulus (signal gain model, Figure 1E), and a model employing hierarchical temporal integration (the HLI model; Figure 1F).

### The Signal Gain Model

It is possible to account for the hierarchical-context-dependence phenomena (P1 and P2; Figure 1D) without invoking distributed temporal integration. Instead, one can offer an explanation based on “signal gain” combined with a qualitative notion of “engagement.” This model makes three assumptions: (1) when participants engage more deeply with a stimulus, the gain of their response to that stimulus increases relative to the noise level, and they produce more reliable neural responses to that stimulus (Cohen et al., 2018; Dmochowski et al., 2012); (2) participants are less “engaged” with temporally scrambled

stimuli than with intact stimuli; and (3) the effects of engagement on neural reliability are larger in higher-order cortical regions. Under these assumptions, the existing empirical data can be explained. First, sensory neocortex would be largely unaffected by engagement (and thus unaffected by scrambling prior context); second, higher-order regions would respond less reliably to scrambled stimuli, and so their intact-versus-scramble correlations would also be decreased (Figure 1E; see STAR Methods). Thus, the signal gain model could explain data from the scrambling experiment, without recourse to any neural representation of temporal context, and it provides an important null model.

### The Hierarchical Linear Integrator (HLI) Model

It is also possible to account for the hierarchical-context-dependence phenomena (P1 and P2; Figure 1D) using a model that explicitly represents and integrates temporal context. We used a linear integration approach inspired by neural integrators in systems neuroscience and mathematical psychology (Huk and Shadlen, 2005; Koulakov et al., 2002; Mazurek et al., 2003; Townsend and Ashby, 1983) and in particular by the seminal “temporal context model” (TCM) in memory research (Howard and Kahana, 2002). In TCM, the arrival of each new stimulus generates linear “drift” of an internal context variable. In particular, if we define the current context as  $CNTX(t)$  and the current input as  $IN(t)$ , a simple form of the update equation for TCM is

$$CNTX(t + 1) = \rho_i CNTX(t) + \beta_i IN(t),$$

where  $\rho_i$  and  $\beta_i$  are parameters that determine the proportion of old and new information in the updated context.

To generate an HLI, we stacked these linear integrator units in stages, and we increased  $\rho$  (and decreased  $\beta$ ) at higher levels of processing. In this way, we increased the proportion of prior information retained at higher stages of the simulated hierarchy. The input to the higher-level integrators was the updated  $CNTX$  vector from the lower-level integrator, generating a cascade of temporal integration (Figure 1F; see STAR Methods).

### Testing Computational Models of Hierarchical Context Dependence

We quantitatively confirmed that both the signal gain model and the hierarchical linear integrator could capture the previously described phenomena (P1 and P2) of hierarchical context dependence (Figures 1D and S2; STAR Methods). Therefore, to provide direct evidence for hierarchical temporal integration (and to rule out the signal gain model), it was necessary to collect more fine-grained measurements of the neural processing of temporally extended sequences.

### Measuring the Moment-by-Moment Construction of Temporal Context

We developed a time-resolved fMRI pattern analysis approach for measuring context-dependent responses to auditory narratives. To understand the time-resolved analysis, consider a case in which two groups of subjects are exposed to the same ~20-s segment of natural speech (e.g., sentence E), but this shared segment is preceded by different speech segments

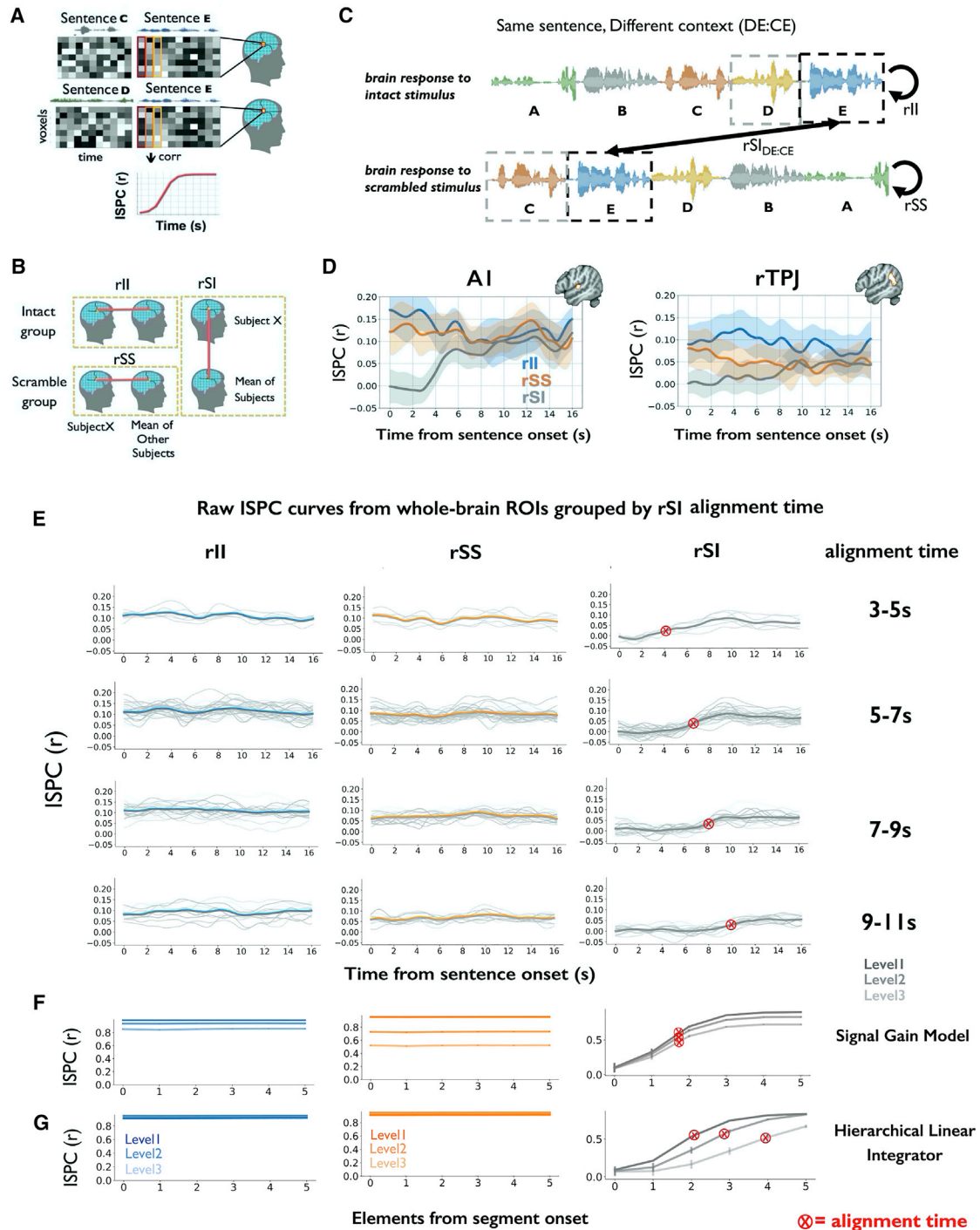


**Figure 2. Gradual Alignment of Responses to a Common Stimulus Preceded by Different Context**

(A) For each sentence, inter-subject pattern correlation (ISPC) was measured by correlating the spatial pattern of activation at each time point across the two groups.

(B) ISPC was calculated between one subject and the average of the rest of the subjects within the intact group (rII), within the scrambled group (rSS) or across the intact and scrambled groups (rSI).

(C) ISPC analysis for the same sentence preceded by different contexts (DE:CE). Here, sentence E followed sentence D for the intact group but it followed sentence C for the scrambled group.

(D) Average ISPC for all sentences in ROIs within an auditory (A1+) region and a right TPJ region. Shaded area indicates a 95% confidence interval on individual rSI estimates.

(legend continued on next page)

across the two groups (e.g., sentence C or sentence D; [Figure 2A](#)). In this setting we can ask how similar the neural responses are within and across these groups, second by second, as they process the shared segment from start to end. At the start of the sentence, the two groups share none of their prior context, but by the end of the sentence, they share much greater amounts of prior context.

To quantify neural similarity within and across groups, we calculated the inter-subject pattern correlation (ISPC) at each time point. Three kinds of ISPC were calculated ([STAR Methods](#)): similarity within the intact group (i.e., intact-intact correlation [rII]), similarity within the scramble group (i.e., scramble-scramble correlation [rSS]), and similarity across the intact and the scramble groups (i.e., intact-scramble correlation [rSI]) ([Figures 2B and 2C](#)).

We first examined the curves of rII, rSS, and rSI within one lower-order region (near A1+; [Figure 2D](#), left) and one higher-order region (near the temporal-parietal junction [TPJ]; [Figure 2D](#), right). In both regions, we observed that (1) the rII and rSS curves were essentially constant from the beginning to the end of a segment; and (2) the rSI curve ramped upward over time, as the intact and scrambled groups were exposed to more and more shared input. These patterns (flat rII, flat rSS, and ramping rSI) are preserved across the cerebral cortex ([Figures 2E and S4A](#)) when we broaden our analysis to a cortex-wide atlas of regions of interest (ROIs) ([Schaefer et al., 2018](#)).

We next examined how the temporal integration profile (rII, rSS, and rSI) differed across regions. To illustrate the basic phenomenon, we examined the rII and rSS curves (within-group correlation) for one sensory region (A1+) and one higher-order region (right TPJ). In A1+, we found that rII and rSS were similar to each other across the whole segments, suggesting that early auditory cortex showed highly reliable responses to the same segments in the two conditions in which the contexts are different ([Figure 2D](#), left). In rTPJ, on the other hand, the rII curve was significantly higher than the rSS ( $t(21) = 2.83$ ,  $p = 0.007$ ,  $t$  test of mean rII and rSS values per segment; [Figure 2D](#), right). The increased response reliability in the TPJ for the intact condition could reflect greater engagement or the fact that the intact stimulus is more familiar. However, the rII and rSS curves do not provide a time-resolved measurement of shared context representation, which can instead be obtained via the across-group correlation (rSI).

The across-group correlation (rSI) ramped upward over time within each story segment, and this ramping occurred later in the higher-order cortex (TPJ) than in sensory cortex (A1+). In A1+, the rSI time course begins to achieve alignment at 4 s after the segment onset, while in TPJ the rSI time course begins to achieve alignment more than 7 s after onset ([Figure 2D](#)). Importantly, the fact that rSI = 0 at the onset of the segment does not necessarily reflect a neural context: the hemodynamics introduce temporal smoothing, carrying signal from the

previous segment into the start of the current segment, even if the underlying neural response is unaffected by context. This hemodynamic artifact makes it difficult to use blood-oxygen-level-dependent (BOLD) imaging to estimate the shortest possible time at which temporal context effects operate. However, the hemodynamics cannot account for the ramping in TPJ occurring more than 3 s later than in A1+. Instead, the later alignment time in TPJ points to a neural context effect, with a longer timescale in higher-order regions. Thus, we tested the generality of this hierarchical pattern by mapping the timescales of context construction across the cerebral cortex.

### Moment-by-Moment Context Analysis Reveals a Hierarchical Organization

The alignment of response across the intact and scramble groups (rSI) increased over time in almost every ROI, and the latency of this ramping differed across brain regions. Because the shape of the rSI curve is not meaningful when the response in the scrambled condition is unreliable, we restricted our analysis of the rSI ramping to the 83 ROIs in which there was a reliable response to the scrambled stimulus (i.e., mean rSS > 0.06; see [STAR Methods](#); [Figure S3A](#)). After confirming that a logistic function could accurately summarize the rSI curves ([Figure S3C](#)), we used logistic fitting to quantify the timescale of rSI ramping in each ROI. We defined the “alignment time” as the time at which the logistic curve reaches its half maximum. We excluded 4 ROIs that were not well fit by a logistic function ([Figure S3B](#)), and 9 ROIs for which alignment times were unreliable (assessed by bootstrapping; [Figure S3D](#); see [STAR Methods](#)). We thus entered 70 ROIs into further analysis. A direct visualization of the raw rSI time courses in each ROI reveals that the logistic fitting accurately captured the profile of the rSI curves and that alignment times differ across areas ([Figures 2E and S4](#)).

Mapping the alignment times across the lateral and medial cortical surface, we observed a “hierarchy of context construction” in the human brain. Early auditory regions first arrive at a shared context-dependent response, followed by consecutive stages of the cortical hierarchy. Alignment times of rSI curves gradually increased from sensory cortex (alignment times ~4 s) toward higher-order regions (alignment times of 10 s or longer; [Figure 3](#), top). Plotting rSI curves along the auditory processing pathway confirmed the hierarchical organization ([Figure 3](#), bottom): lower-level regions (e.g., A1+) quickly arrived at a shared response between intact and scrambled groups, while regions in inferior parietal and medial parietal cortex took longer to align across the intact and scrambled groups.

### Hierarchical Integrator Model Predicts Hierarchical Context Construction

The results of hierarchical context construction rule out the signal gain model, because it could not account for different

(E) The rII, rSS, and rSI<sub>DE:CE</sub> curves are shown for individual regions, grouped by “alignment time.” The individual region curves are pale gray, while mean curves for each group of regions is in thick blue (rII), orange (rSS), and gray (rSI<sub>DE:CE</sub>). Note that the rII and rSS curves do not ramp, either for the mean curve or for individual regions, while the rSI curves show ramping in almost all regions.

(F) Simulation of rII, rSS, and rSI for the signal gain model. The rSI curves exhibit ramping, but the alignment times are stable across levels.

(G) Simulation of rSS and rSI for the HLI model. The alignment time is greater in higher levels of the HLI model. A1, primary auditory cortex; rTPJ, right temporal-parietal junction.

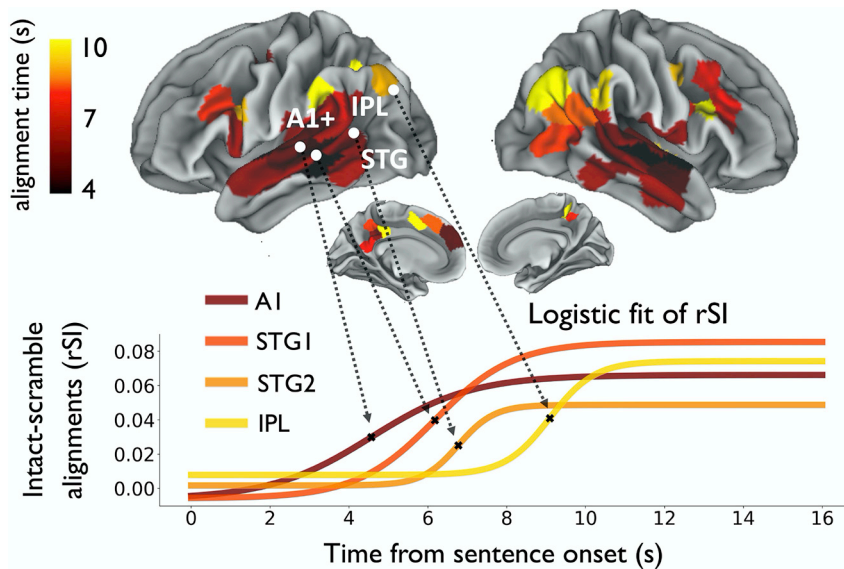


**Figure 3. Hierarchical Timescales of Context Construction across the Human Cerebral Cortex**

Cortical map of the timescale at which neural responses align to a common input preceded by different contexts (top). Alignment time is quantified as the time for each  $rSI_{DE:CE}$  curve to reach half its maximum value. Fitted logistic curves for four representative ROIs along the cortical hierarchy (bottom). A1, primary auditory cortex; IPL, inferior parietal lobe; rSI, intact-scramble ISPC; STG, superior temporal gyrus.

rates of context construction at different levels of the cortex (Figure 2F). On the other hand, the HLI model could account for these inter-regional differences, because its higher-level integrators have longer time constants; the rSI curves in the HLI model ramp upward later for higher-level linear integrators (Figure 2G;  $t = -104$ ,  $p < 0.0001$ ), and this effect is magnified by the fact that the integrators are stacked in a hierarchy (Figure S5C; Table S1).

Because the signal gain model can capture variations in the mean level of the rII and rSS curves and the asymptotic height of each rSI curve (which may reflect variation in engagement across the intact and scrambled stimuli) (Figure 2F), the signal gain mechanisms should still be considered as a component of future models. However, the dominant pattern in our data (the hierarchical variation in alignment times) requires a model that maintains temporal context to varying degrees across regions.

### Time-Resolved Analysis of Context Forgetting

The time-resolved pattern analysis indicates that information is temporally integrated second by second throughout the cortex. But is integrating information from the past always desirable? For example, if the subject of a new sentence is unrelated to the verb of the previous sentence, then perhaps we might want to separate these pieces of information rather than integrate them. Therefore, in addition to the process of integrating information over time, we also measured the neural process of separating information from distinct events.

We have already shown that the two groups will gradually construct an aligned mental context and begin to respond in the same way to common input (Figure 4A, middle), but what happens when the common input ends? At this moment, the two groups begin to hear different inputs, and yet these different inputs are preceded by the shared context. We expect that the two groups should gradually “forget” the previously shared mental context, but its influence may persist for some time (Figure 4A, right).

(STAR Methods). This leads to a testable prediction: if temporal integration within each region has a fixed time constant, then regions which integrate information more slowly (i.e., higher-order regions) should also forget prior information more slowly. Thus, we can test the class of linear integrator models by testing whether rates of contextual alignment and separation are correlated across regions.

Contrary to the predictions of linear integrator models, rates of alignment and separation were uncorrelated in the human cerebral cortex. We operationalized the “forgetting” of shared context as the “separation time” of neural responses that begin with a common context. The separation time was measured analogously to alignment time: how quickly neural responses diverge when participants processed different input preceded by a shared prior context. To visualize the relationship between context construction and forgetting, we grouped brain regions according to their alignment time ( $rSI_{CONSTRUCT}$  or  $rSI_{DE:CE}$ ) and then visualized the rate at which they forgot prior information ( $rSI_{FORGET}$  or  $rSI_{CD:CE}$ ). The  $rSI_{FORGET}$  curves decreased at a similar rate, regardless of whether the corresponding  $rSI_{CONSTRUCT}$  curve had a fast or a slow alignment time (Figure 4D). Moreover, we observed no correlation between alignment time and separation time across ROIs ( $r = -0.13$ ,  $p = 0.33$ ; Figure S5B). This decoupling of alignment times and separation times cannot be explained by fixed-rate linear integrator models, such as HLI, in which the correlation between alignment times and separation times is very strong ( $r = 0.99$ ; Figure S5B).

### Gated Integration Using HAT

The mismatch of alignment and separation times in cortical dynamics indicates that the integration rate is variable, consistent with the notion that temporal sequences are grouped into events, and that prior context is more rapidly forgotten at event boundaries (Reynolds et al., 2007; Zacks and Tversky, 2001). Therefore, we set out to develop a model that can account for the existing data on hierarchical temporal processing while

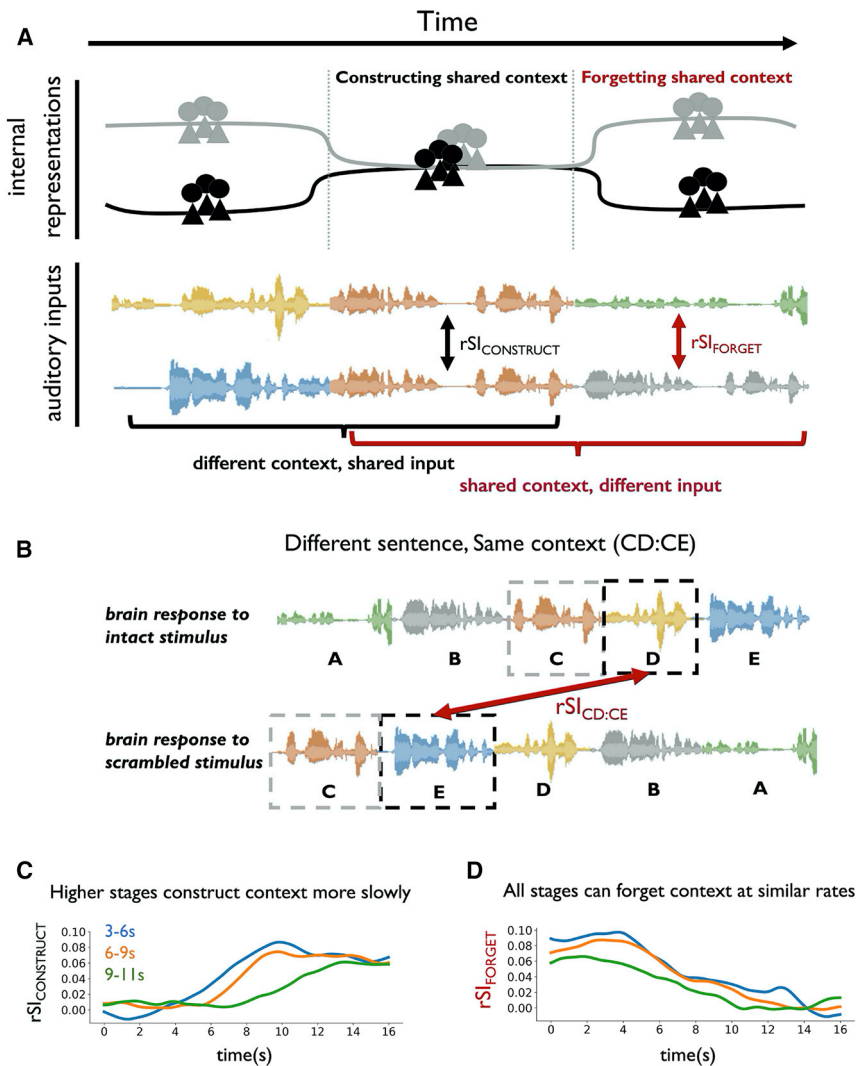


**Figure 4. Distinct Timescales of Alignment and Separation in Cortical Dynamics**

(A) Schematic of internal representations falling into and out of alignment as common and distinct inputs are presented. Two groups gradually construct a shared context when they listen to the same input preceded by different contexts, and thus their neural responses fall into alignment. When common input ends, the two groups begin to process a distinct input preceded by a shared context, and participants forget this shared context over time. (B) Schematic of ISPC analysis, when different speech segments are preceded by the same context. Here, segment D in the intact group and segment E in the scramble group were both preceded by segment C (CD:CE). (C) Empirical  $rSI_{DE:CE}$  results grouped by alignment time of 3–6 s, 6–9 s, and 9–11 s. (D) Empirical  $rSI_{CD:CE}$  results, using the same region groupings from the  $rSI_{DE:CE}$  results in (C). Regions at different levels of cortical hierarchy can forget context at similar rates.  $rSI$ , intact-scramble ISPC.

### HAT Captures Empirical Patterns of Context Construction and Forgetting

The HAT model successfully captured the hierarchical context dependence phenomenon (Figure S2G). Moreover, HAT exhibited an important advantage over the signal gain model and HLI model in that its ability to integrate information over time was more selective for previously learned sequences (STAR Methods; Figures S2C, S2E, and S2G; model by training interaction  $\eta^2 = 0.37$ ). In fact, integration in the full HAT model was more learning dependent than any other model tested, including linear integrator variants and

also providing mechanisms for grouping temporal sequences. We developed the HAT model, which employs a nonlinear and gated approach to temporal integration. The HAT model was inspired by TRACX2, a recurrent network model of human sequence learning (French et al., 2011; Mareschal and French, 2017).

The HAT model is composed of a stack of “autoencoder in time” (AT) units (Figure 5B; details in STAR Methods). At each time step, each AT unit attempts to generate a simplified, or compressed, joint representation (hidden representation [HID]) of its current input (IN) and its prior context (CNTX; Figure S1). The higher-order AT units possess longer intrinsic timescale  $\tau$ , so their context is less influenced by their input at each moment (Figure 5C). Also, the proportion of present input that is combined with prior context (and transmitted from a lower AT unit to a higher AT unit) depends on a reconstruction error (or “surprise”),  $\alpha$ , which is computed locally within each AT unit (Figure 5D). In sum, the HAT model performs a nonlinear (compressive) integration of its context representation with each input, and this integration is gated by surprise.

HAT variants (Figure S5C; Table S1). We analyze the HAT model further in Supplemental Information (Figures S2 and S5; Table S1).

The HAT model also captured the empirical result that higher-level regions construct new context more slowly than sensory regions (delayed ramping in  $rSI_{DE:CE}$  or  $rSI_{CONSTRUCT}$ ; Figure 5F). Moreover, because the HAT model can prevent the integration of prior context with new information (using its context gating mechanism), the influence of prior context could be reduced at moments of high surprise (Figures 5D, 5E, S2K, and S2L). Therefore, while the HLI model predicts that regions that slowly integrate input must also slowly forget prior context (Figure 5H), the HAT model predicts that higher-level regions need not forget prior information more slowly (Figure 5I). Thus, HAT provided predictions most consistent with all of our empirical results (see also Figure S5C; Table S1).

We have shown that HAT model can account for two new empirical phenomena: hierarchical variation in the alignment time during processing of a shared input (Figures 2 and 3) and the decoupling of alignment-timescales and separation-timescales (Figures 4 and 5). But what are the essential computational

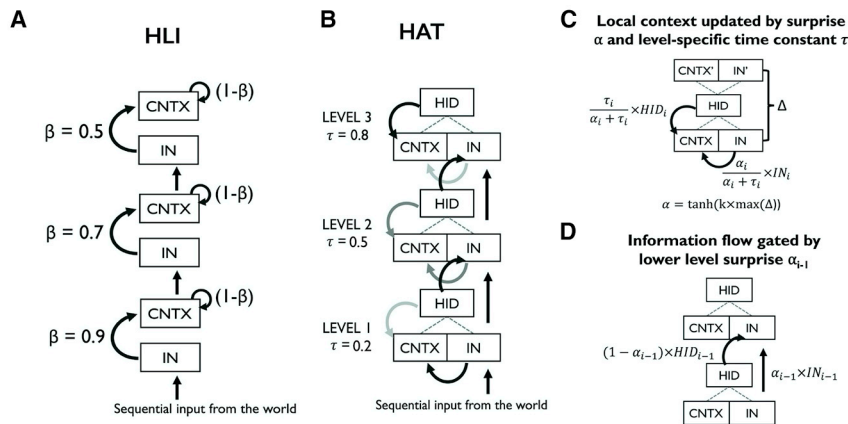


**Figure 5. Modeling Context Construction and Context Forgetting**

(A) HLI model schematic. The new state of each unit is a linear weighted sum of its old state and its new input. (B) HAT model schematic. Each region maintains a representation of temporal context, which is combined with new input to form a simplified joint representation.

(C) An AT unit, in which local context CNTX is updated via hidden representation HID and current input IN, modulated by time constant  $\tau$  and “surprise”  $\alpha$ .  $\alpha$  is computed via auto-associative error,  $\Delta$ , and a scaling parameter,  $k$ .

(D) In HAT, the input to level  $i$  is gated by surprise  $\alpha$  from level  $(i - 1)$ .

(E) HLI simulation of  $rSI_{DE:CE}$  predicts longer alignment time at higher stages of processing. Error bars indicate 95% confidence intervals of the mean, where the mean is computed across segments within a simulation.

(F) HAT simulation of  $rSI_{DE:CE}$  predicts longer alignment time at higher stages of processing.

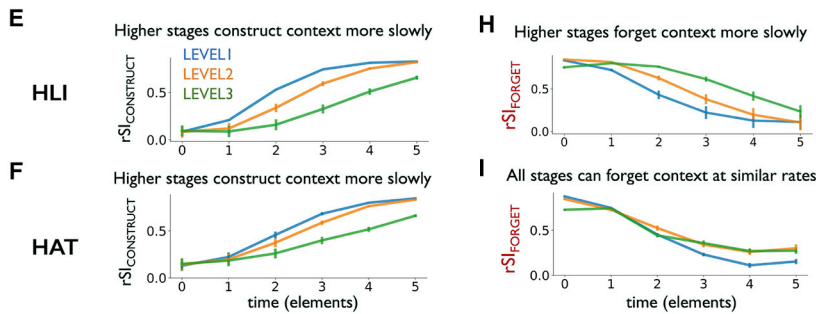
(G) Empirical  $rSI_{DE:CE}$  results grouped by alignment time, consistent with predictions of both HLI and HAT.

(H) HLI simulation of  $rSI_{CD:CE}$  predicts that regions that construct context slowly will also forget context slowly.

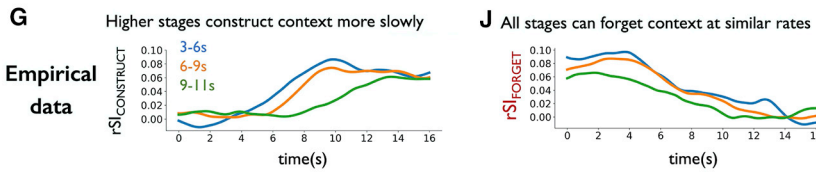
(I) HAT simulations predict that the timescale of context separation ( $rSI_{CD:CE}$ ) need not be slower in levels of the model with longer alignment times ( $rSI_{DE:CE}$ ).

(J) Empirical  $rSI_{CD:CE}$  results grouped by alignment time. AT, autoencoder in time; HAT, hierarchical autoencoders in time; rSI, intact-scramble ISPC.

**Model Predictions**



**Empirical Results**



elements required to account for these data? Although it is difficult to determine necessity in general, we tested an ensemble of model variants and found that the gating of integration was a necessary component, within this ensemble, to explain the data. Moreover, both hierarchical architecture and nonlinearity of integration increased the sensitivity of all models to prior temporal context (Table S1; Figure S5; STAR Methods).

**DISCUSSION**

The theory of hierarchical timescales in the cerebral cortex is influential across cognitive, systems, and clinical neuroscience (Baldassano et al., 2017; Burt et al., 2018; Chaudhuri et al., 2015; Chen et al., 2016; Cocchi et al., 2016; Demirtaş et al., 2019; Fuster, 1997; Hasson et al., 2008, 2015; Himberger et al., 2018; Kiebel et al., 2008; Murray et al., 2014; Runyan et al., 2017; Scott et al., 2017; Simony et al., 2016; Wasmuht et al., 2018; Watanabe et al., 2019; Yeshurun et al., 2017; Zuo et al., 2020). The intrinsic timescales of brain dynamics are longer in higher-order areas, as shown by single-unit data in macaques

elements of timescales in brain dynamics are correlated with gradients of myelin density (Glasser and Van Essen, 2011), gene transcription (Burt et al., 2018), and anatomical connectivity (Margulies et al., 2016). Moreover, accounting for regional variation in timescales improves the prediction of human functional connectivity (Demirtaş et al., 2019), and individual differences in timescales predict clinical behavioral symptoms (Watanabe et al., 2019).

Despite these advances in our understanding of hierarchical cortical dynamics, our models of the associated information processing have remained phenomenological. What are the computations that integrate past and present information within the hierarchical networks of our brains? Here, we used a new approach to measure the construction and forgetting of temporal context in the human brain, and we used these data to constrain computational models of hierarchical temporal integration.

Our ISPC analysis revealed a phenomenon of “hierarchical context construction”: when two participants heard the same sentence preceded by different contexts, their neural responses

gradually aligned. The responses aligned earliest in early sensory cortices, followed by secondary cortices, and some higher-order regions did not align until participants shared 10 s of continuous common input. This phenomenon of hierarchical context construction suggests the existence of a distributed and multi-scale representation of prior context, which affects the neural response to input at each moment. The existence of a distributed context representation is consistent with the finding that recurrent neural networks provide a better prediction of visual pathway responses than feedforward models (Kietzmann et al., 2019; Shi et al., 2018), especially for the later component of the neural response (Kar et al., 2019).

Regional variations in hemodynamic peaks (~1–2 s between sensory and higher-order cortices; Belin et al., 1999; Handwerker et al., 2004) cannot account for the 8-s inter-regional variation we observed in alignment time (Figure S4B). Additionally, if a hemodynamic delay increased the alignment time in a particular region, then this should also delay its separation time, leading to a positive correlation between alignment and separation times, but this was not observed (Figure S5B).

Regions do not “forget” context at the same rate as they “construct” context (Figures 5E and 5H). This implies the existence of a mechanism for flexibly altering how the past influences present responses. Linear integrator models lack such flexibility; the rate of contextual alignment and the rate of separation are both inversely related to a fixed parameter,  $\rho$ , and so the past and present information are linearly mixed in the same way regardless of their content. By contrast, models such as HAT can flexibly modulate how prior context is integrated with new input. In HAT, if prior context can be successfully compressed with new input, then information about context is preserved, but if prior context and new input are incompatible (leading to prediction error), then the context is overwritten (Mareschal and French, 2017). A distributed and surprise-driven “context gating” mechanism is consistent with evidence for pattern violations being signaled at multiple levels of cortical processing (Bekinschtein et al., 2009; Himberger et al., 2018; Wacongne et al., 2011).

Context gating is important for clearing out irrelevant prior information at the boundaries between chunks or events (DuBrow et al., 2017; Ezzayat and Davachi, 2011; Reynolds et al., 2007). Baldassano et al. (2017) revealed that almost all stages of cortical processing are sensitive to event structure, with sensory regions changing rapidly at the boundaries between shorter events (e.g., eating a piece of food) and higher-order regions changing at the boundaries between longer events (e.g., having an entire meal). However, because the immediate stimulus and its preceding context always covaried, it was uncertain whether rapid cortical state changes reflected rapid changes in input, rapid changes in contextual influence, or both. Here, by separately controlling current input and prior context, we demonstrated that with the sharp event boundaries introduced in our stimuli, the local context could be gated at those boundaries. The gating of context may be driven by an immediate prediction error, as in the HAT model, or via a more diffuse breakdown of temporal associations (Schapiro et al., 2013)

At a computational level, context gating is widely used in processing information sequences and in easing learning. Gated

neural networks can capture long-range temporal dependencies in sequence learning tasks (Hochreiter and Schmidhuber, 1997). Combining gated neural networks with structured probabilistic inference can generate human-like event segmentation of natural video input (Franklin et al., 2019). Moreover, gating is a broadly useful process in biological models of working memory, both for preventing sensory interference with maintained information and for flexible updating and integration (Carpenter and Grossberg, 1987; Heeger and Mackey, 2018; O’Reilly and Frank, 2006), and disturbances in gating mechanisms may manifest in severe cognitive deficits (Braver et al., 1999).

Our computational approach was inspired by the neurocognitive models of Botvinick, (2007) and Kiebel et al. (2008), in which higher stages of cortical processing learned or controlled temporal structure at longer timescales. More generally, multi-scale machine-learning architectures have been proposed for reducing the complexity of the learning problem at each scale and for representing multi-scale environments (Chung et al., 2016; Jaderberg et al., 2019; Mozer, 1992; Mujika et al., 2017; Quax et al., 2019; Schmidhuber, 1992). In neuroscience, multiple timescale representations have been proposed for learning value functions (Sutton, 1995), tracking reward (Bernacchia et al., 2011), and perceiving and controlling action (Botvinick, 2007; Paine and Tani, 2005). Moreover, the concept of temporal “grain” is influential in theories of hippocampal organization (Brunec et al., 2018; Momennejad and Howard, 2018; Poppenk et al., 2013; Shankar et al., 2016) and cortical organization (Baldassano et al., 2017; Fuster, 1997; Hasson et al., 2015; Lü et al., 1992; Wacongne et al., 2011). Consistent with hierarchical timescale models, we find that more temporally extended representations are learned in higher stages of cortical processing, where dynamics change more slowly. These data constrain future models by revealing the moment-by-moment time course of context construction in the cerebral cortex and demonstrating that slowly evolving context representations can be rapidly updated at event boundaries.

### Limitation and Future Directions

For parsimony, we modeled temporal integration using only within-layer recurrence (i.e., without inter-regional recurrence), but there is rich anatomical reciprocity in the brain (Bastos et al., 2012; Markov et al., 2013; Sporns et al., 2007), and many models of cortical function emphasize the importance of feedback and top-down prediction (Friston and Kiebel, 2009; Heeger, 2017; Heeger and Mackey, 2018; Kietzmann et al., 2019; Rao and Ballard, 1999). It is not clear which expectation effects in temporal processing rely on top-down predictions from high-level representations as opposed to more local recurrent integration or facilitation (e.g., Ferreira and Chantavarin, 2018). Long-range feedback is essential for some brain functions (e.g., attentional control and imagery), and models with (weak) long-range feedback could account for our data. Still, the local recurrence of the HAT model was sufficient to account for the integration processes we measured during narrative comprehension. Also, feedforward signaling in the HAT model does depend on the magnitude of layer-local surprise, which is a feature in common with predictive coding model.

The gating and learning in the HAT model are much less flexible than in many machine-learning architectures (e.g., long-short-term-memory networks [LSTMs] and gated recurrent units [GRUs]). Gates in neural networks (such as forget gates in LSTMs or update gates in GRUs) can be triggered by arbitrary states elsewhere in the network, but the gating in HAT is determined entirely by a local prediction error. Additionally, learning in HAT is layer local, rather than end to end. The locality of the HAT model adds to its biological plausibility, but future work should test the necessity of more powerful forms of gating and event learning for capturing human sequence processing.

In future work, we will train HAT variants on linguistic corpora and use these to generate context-aware encoding models of the neural response to complex language (e.g., [Jain and Huth, 2018](#)). Encoding models quantitatively predict the neural response at each moment, providing a comparison against the full richness of the data; at the same time, powerful encoding models may also be more difficult to mechanistically interpret. More generally, three important questions for future work will be (1) whether gating of past context is binary or graded, depending on the magnitude of local prediction error; (2) whether context gating can occur entirely independently across distinct levels of processing; and (3) how the context gradient we observed relates to local neuronal processes on the sub-second scale ([Demirtaş et al., 2019](#); [Goris et al., 2014](#); [Norman-Haignere et al., 2019](#); [Zhou et al., 2018](#)).

To recap, we showed that brain regions aligned, second by second, in a hierarchical gradient, when they were exposed to a common input preceded by distinct contexts. We ruled out explanations of this phenomenon based on stimulus engagement or fixed-rate integration processes. Our models and data provide concrete constraints for models of brain function in which memory is inherent to perceptual and cognitive function ([Buonomano and Maass, 2009](#); [Frost et al., 2015](#); [Fuster, 1997](#); [Hasson et al., 2015](#); [McClelland and Rumelhart, 1985](#); [Shi et al., 2018](#)), and we suggest general principles, nonlinear integration and gating, that are used in temporal information processing across the cortical hierarchy.

## STAR★METHODS

Detailed methods are provided in the online version of this paper and include the following:

- **KEY RESOURCES TABLE**
- **LEAD CONTACT AND MATERIALS AVAILABILITY**
- **EXPERIMENTAL MODEL AND SUBJECT DETAILS**
  - Subjects
  - Acquiring and Preprocessing of Neuroimaging Data
- **METHOD DETAILS**
  - Linear Integrator Models
  - Parallel Linear Integrator Model: PLI
  - Hierarchical Linear Integrator Model: HLI
  - The Signal Gain Model
  - Hierarchical Autoencoders in Time: HAT Model
  - HAT variants
  - Model Simulations and Predictions
  - Analysis of Linear Integrators
  - Empirical Measurements of Context Dependence

- **QUANTIFICATION AND STATISTICAL ANALYSIS**
  - Quantifying context dependence in models
  - Validating neural response reliability
  - Quantifying alignment time
  - Quantifying separation time
  - Simulating alignment time and separation time
- **DATA AND CODE AVAILABILITY**

## SUPPLEMENTAL INFORMATION

Supplemental Information can be found online at <https://doi.org/10.1016/j.neuron.2020.02.013>.

## ACKNOWLEDGMENTS

The authors gratefully acknowledge the support of the National Institutes of Mental Health (grant R01MH119099 to C.J.H. and grant R01 MH111439-01 subawarded to C.J.H.), the NVIDIA Corporation (GPU grant), the Sloan Foundation (research fellowship to C.J.H.), and the Government of Taiwan (graduate scholarship to H.-Y.S.C.). We thank Janice Chen, Ken Norman, Anna Schapiro, Hongmi Lee, Uri Hasson, Sam Nastase, Jinhan Zhang, and Zoey Zuo for their insightful feedback and discussion.

## AUTHOR CONTRIBUTIONS

Conceptualization, H.-Y.S.C. and C.J.H.; Methodology, H.-Y.S.C. and C.J.H.; Formal Analysis, H.-Y.S.C. and C.J.H.; Investigation, H.-Y.S.C. and C.J.H.; Resources, H.-Y.S.C. and C.J.H.; Writing – Original Draft, H.-Y.S.C. and C.J.H.; Visualization, H.-Y.S.C.; Supervision, C.J.H.; Funding Acquisition, H.-Y.S.C. and C.J.H.

## DECLARATION OF INTERESTS

The authors declare no competing interests.

Received: August 7, 2019  
Revised: December 23, 2019  
Accepted: February 11, 2020  
Published: March 11, 2020

## REFERENCES

- Baldassano, C., Chen, J., Zadbood, A., Pillow, J.W., Hasson, U., and Norman, K.A. (2017). Discovering event structure in continuous narrative perception and memory. *Neuron* 95, 709–721.e5.
- Bastos, A.M., Usrey, W.M., Adams, R.A., Mangun, G.R., Fries, P., and Friston, K.J. (2012). Canonical microcircuits for predictive coding. *Neuron* 76, 695–711.
- Bekinschtein, T.A., Dehaene, S., Rohaut, B., Tadel, F., Cohen, L., and Naccache, L. (2009). Neural signature of the conscious processing of auditory regularities. *Proc. Natl. Acad. Sci. USA* 106, 1672–1677.
- Belin, P., Zatorre, R.J., Hoge, R., Evans, A.C., and Pike, B. (1999). Event-related fMRI of the auditory cortex. *Neuroimage* 10, 417–429.
- Bernacchia, A., Seo, H., Lee, D., and Wang, X.J. (2011). A reservoir of time constants for memory traces in cortical neurons. *Nat. Neurosci.* 14, 366–372.
- Botvinick, M.M. (2007). Multilevel structure in behaviour and in the brain: a model of Fuster's hierarchy. *Philos. Trans. R. Soc. Lond. B Biol. Sci.* 362, 1615–1626.
- Braver, T.S., Barch, D.M., and Cohen, J.D. (1999). Cognition and control in schizophrenia: a computational model of dopamine and prefrontal function. *Biol. Psychiatry* 46, 312–328.
- Brunec, I.K., Bellana, B., Ozubko, J.D., Man, V., Robin, J., Liu, Z.X., Grady, C., Rosenbaum, R.S., Winocur, G., Barense, M.D., and Moscovitch, M. (2018). Multiple scales of representation along the hippocampal anteroposterior axis in humans. *Curr. Biol.* 28, 2129–2135.e6.

- Buonomano, D.V., and Maass, W. (2009). State-dependent computations: spatiotemporal processing in cortical networks. *Nat. Rev. Neurosci.* *10*, 113–125.
- Burt, J.B., Demirtaş, M., Eckner, W.J., Navejar, N.M., Ji, J.L., Martin, W.J., Bernacchia, A., Anticevic, A., and Murray, J.D. (2018). Hierarchy of transcriptional specialization across human cortex captured by structural neuroimaging topography. *Nat. Neurosci.* *21*, 1251–1259.
- Carpenter, G.A., and Grossberg, S. (1987). A massively parallel architecture for a self-organizing neural pattern recognition machine. *Comput. Vis. Graph. Image Process.* *37*, 54–115.
- Chaudhuri, R., Knoblauch, K., Gariel, M.A., Kennedy, H., and Wang, X.J. (2015). A large-scale circuit mechanism for hierarchical dynamical processing in the primate cortex. *Neuron* *88*, 419–431.
- Chen, J., Honey, C.J., Simony, E., Arcaro, M.J., Norman, K.A., and Hasson, U. (2016). Accessing real-life episodic information from minutes versus hours earlier modulates hippocampal and high-order cortical dynamics. *Cereb. Cortex* *26*, 3428–3441.
- Chung, J., Ahn, S., and Bengio, Y. (2016). Hierarchical multiscale recurrent neural networks. *arXiv*, 1609.01704 <https://arxiv.org/abs/1609.01704>.
- Cocchi, L., Sale, M.V.L., Lollo, L., Bell, P.T., Nguyen, V.T., Zalesky, A., Breakspear, M., and Mattingley, J.B. (2016). A hierarchy of timescales explains distinct effects of local inhibition of primary visual cortex and frontal eye fields. *eLife* *5*, e15252.
- Cohen, S.S., Madsen, J., Touchan, G., Robles, D., Lima, S.F.A., Henin, S., and Parra, L.C. (2018). Neural engagement with online educational videos predicts learning performance for individual students. *Neurobiol. Learn. Mem.* *155*, 60–64.
- Demirtaş, M., Burt, J.B., Helmer, M., Ji, J.L., Adkinson, B.D., Glasser, M.F., Van Essen, D.C., Sotiropoulos, S.N., Anticevic, A., and Murray, J.D. (2019). Hierarchical heterogeneity across human cortex shapes large-scale neural dynamics. *Neuron* *101*, 1181–1194.e13.
- Dmochowski, J.P., Sajda, P., Dias, J., and Parra, L.C. (2012). Correlated components of ongoing EEG point to emotionally laden attention - a possible marker of engagement? *Front. Hum. Neurosci.* *6*, 112.
- DuBrow, S., Rouhani, N., Niv, Y., and Norman, K.A. (2017). Does mental context drift or shift? *Curr. Opin. Behav. Sci.* *17*, 141–146.
- Ezzyat, Y., and Davachi, L. (2011). What constitutes an episode in episodic memory? *Psychol. Sci.* *22*, 243–252.
- Ferreira, F., and Chantavarin, S. (2018). Integration and prediction in language processing: a synthesis of old and new. *Curr. Dir. Psychol. Sci.* *27*, 443–448.
- Franklin, N., Norman, K.A., Ranganath, C., Zacks, J.M., and Gershman, S.J. (2019). Structured event memory: a neuro-symbolic model of event cognition. *bioRxiv*. <https://doi.org/10.1101/541607>.
- French, R.M., Addyman, C., and Mareschal, D. (2011). TRACX: a recognition-based connectionist framework for sequence segmentation and chunk extraction. *Psychol. Rev.* *118*, 614–636.
- Friston, K., and Kiebel, S. (2009). Predictive coding under the free-energy principle. *Philos. Trans. R. Soc. Lond. B Biol. Sci.* *364*, 1211–1221.
- Frost, R., Armstrong, B.C., Siegelman, N., and Christiansen, M.H. (2015). Domain generality versus modality specificity: the paradox of statistical learning. *Trends Cogn. Sci.* *19*, 117–125.
- Fuster, J.M. (1997). Network memory. *Trends Neurosci.* *20*, 451–459.
- Gibson, J.J., Reed, E.S., and Jones, R. (1982). *Reasons for Realism: Selected Essays of James J. Gibson* (Lawrence Erlbaum Assoc.).
- Glasser, M.F., and Van Essen, D.C. (2011). Mapping human cortical areas in vivo based on myelin content as revealed by T1- and T2-weighted MRI. *J. Neurosci.* *31*, 11597–11616.
- Goris, R.L.T., Movshon, J.A., and Simoncelli, E.P. (2014). Partitioning neuronal variability. *Nat. Neurosci.* *17*, 858–865.
- Handwerker, D.A., Ollinger, J.M., and D'Esposito, M. (2004). Variation of BOLD hemodynamic responses across subjects and brain regions and their effects on statistical analyses. *Neuroimage* *21*, 1639–1651.
- Hasson, U., Nir, Y., Levy, I., Fuhrmann, G., and Malach, R. (2004). Intersubject synchronization of cortical activity during natural vision. *Science* *303*, 1634–1640.
- Hasson, U., Yang, E., Vallines, I., Heeger, D.J., and Rubin, N. (2008). A hierarchy of temporal receptive windows in human cortex. *J. Neurosci.* *28*, 2539–2550.
- Hasson, U., Chen, J., and Honey, C.J. (2015). Hierarchical process memory: memory as an integral component of information processing. *Trends Cogn. Sci.* *19*, 304–313.
- He, B.J. (2011). Scale-Free Properties of the Functional Magnetic Resonance Imaging Signal during Rest and Task. *J. Neurosci.* *31*, 13786–13795.
- Heeger, D.J. (2017). Theory of cortical function. *Proc. Natl. Acad. Sci. USA* *114*, 1773–1782.
- Heeger, D.J., and Mackey, W.E. (2018). ORGaNICs: a canonical neural circuit computation. *bioRxiv*. <https://doi.org/10.1101/506337>.
- Himberger, K.D., Chien, H.Y., and Honey, C.J. (2018). Principles of temporal processing across the cortical hierarchy. *Neuroscience* *389*, 161–174.
- Hochreiter, S., and Schmidhuber, J. (1997). Long short-term memory. *Neural Comput.* *9*, 1735–1780.
- Honey, C.J., Thesen, T., Donner, T.H., Silbert, L.J., Carlson, C.E., Devinsky, O., Doyle, W.K., Rubin, N., Heeger, D.J., and Hasson, U. (2012). Slow cortical dynamics and the accumulation of information over long timescales. *Neuron* *76*, 423–434.
- Howard, M.W., and Kahana, M.J. (2002). A distributed representation of temporal context. *J. Math. Psychol.* *46*, 269–299.
- Huk, A.C., and Shadlen, M.N. (2005). Neural activity in macaque parietal cortex reflects temporal integration of visual motion signals during perceptual decision making. *J. Neurosci.* *25*, 10420–10436.
- Jaderberg, M., Czarnecki, W.M., Dunning, I., Marris, L., Lever, G., Castañeda, A.G., Beattie, C., Rabinowitz, N.C., Morcos, A.S., Ruderman, A., et al. (2019). Human-level performance in 3D multiplayer games with population-based reinforcement learning. *Science* *364*, 859–865.
- Jain, S., and Huth, A. (2018). Incorporating context into language encoding models for fMRI. In *NIPS'18: Proceedings of the 32nd International Conference on Neural Information Processing Systems*, pp. 6628–6637.
- Kar, K., Kubilius, J., Schmidt, K., Issa, E.B., and DiCarlo, J.J. (2019). Evidence that recurrent circuits are critical to the ventral stream's execution of core object recognition behavior. *Nat. Neurosci.* *22*, 974–983.
- Kiebel, S.J., Daunizeau, J., and Friston, K.J. (2008). A hierarchy of time-scales and the brain. *PLoS Comput. Biol.* *4*, e1000209.
- Kietzmann, T.C., Spoerer, C.J., Sørensen, L.K.A., Cichy, R.M., Hauk, O., and Kriegeskorte, N. (2019). Recurrence is required to capture the representational dynamics of the human visual system. *Proceedings of the National Academy of Sciences of the United States of America* *116*, 21854–21863.
- Koulakov, A.A., Raghavachari, S., Kepecs, A., and Lisman, J.E. (2002). Model for a robust neural integrator. *Nat. Neurosci.* *5*, 775–782.
- Lerner, Y., Honey, C.J., Silbert, L.J., and Hasson, U. (2011). Topographic mapping of a hierarchy of temporal receptive windows using a narrated story. *J. Neurosci.* *31*, 2906–2915.
- Lü, Z.L., Williamson, S.J., and Kaufman, L. (1992). Human auditory primary and association cortex have differing lifetimes for activation traces. *Brain Res.* *572*, 236–241.
- Mareschal, D., and French, R.M. (2017). TRACX2: a connectionist autoencoder using graded chunks to model infant visual statistical learning. *Philos. Trans. R. Soc. Lond. B Biol. Sci.* *372*, 20160057.
- Margulies, D.S., Ghosh, S.S., Goulas, A., Falkiewicz, M., Huntenburg, J.M., Langs, G., Bezgin, G., Eickhoff, S.B., Castellanos, F.X., Petrides, M., et al. (2016). Situating the default-mode network along a principal gradient of macroscale cortical organization. *Proc. Natl. Acad. Sci. USA* *113*, 12574–12579.

- Markov, N.T., Ercsey-Ravasz, M., Van Essen, D.C., Knoblauch, K., Toroczkai, Z., and Kennedy, H. (2013). Cortical high-density counterstream architectures. *Science* **342**, 1238406–1238406.
- Mazurek, M.E., Roitman, J.D., Ditterich, J., and Shadlen, M.N. (2003). A role for neural integrators in perceptual decision making. *Cereb. Cortex* **13**, 1257–1269.
- McClelland, J.L., and Rumelhart, D.E. (1985). Distributed memory and the representation of general and specific information. *J. Exp. Psychol. Gen.* **114**, 159–197.
- Momennejad, I., and Howard, M.W. (2018). Predicting the future with multi-scale successor representations. *bioRxiv*. <https://doi.org/10.1101/449470>.
- Mozer, M. (1992). Induction of multiscale temporal structure. *Adv. Neural Inf. Process. Syst.* **4**, 275–282.
- Mujika, A., Meier, F., and Steger, A. (2017). Fast-slow recurrent neural networks. *arXiv* <https://arxiv.org/abs/1705.08639>.
- Murray, J.D., Bernacchia, A., Freedman, D.J., Romo, R., Wallis, J.D., Cai, X., Padoa-Schioppa, C., Pasternak, T., Seo, H., Lee, D., and Wang, X.J. (2014). A hierarchy of intrinsic timescales across primate cortex. *Nat. Neurosci.* **17**, 1661–1663.
- Nastase, S.A., Liu, Y.F., Hillman, H., Zadbood, A., Hasenfratz, L., Keshavarzian, N., Chen, J., Honey, C.J., Yeshurun, Y., Regev, M., et al. (2019). fMRI data for evaluating models of naturalistic language comprehension. <https://openneuro.org/datasets/ds002345/versions/1.0.1>.
- Norman-Haignere, S., Long, L., Devinsky, O., Doyle, W., McKhann, G., Schevon, C., Flinker, A., and Mesgarani, N. (2019). Temporal context invariance reveals neural processing timescales in human auditory cortex. In *Proceedings of the 2019 Conference on Cognitive Computational Neuroscience (2019 Conference on Cognitive Computational Neuroscience)*.
- O'Reilly, R.C., and Frank, M.J. (2006). Making working memory work: a computational model of learning in the prefrontal cortex and basal ganglia. *Neural Comput.* **18**, 283–328.
- Ogawa, T., and Komatsu, H. (2010). Differential temporal storage capacity in the baseline activity of neurons in macaque frontal eye field and area V4. *J. Neurophysiol.* **103**, 2433–2445.
- Paine, R.W., and Tani, J. (2005). How hierarchical control self-organizes in artificial adaptive systems. *Adapt. Behav.* **13**, 211–225.
- Poeppl, D. (2003). The analysis of speech in different temporal integration windows: cerebral lateralization as 'asymmetric sampling in time'. *Speech Commun.* **41**, 245–255.
- Poppenk, J., Evensmoen, H.R., Moscovitch, M., and Nadel, L. (2013). Long-axis specialization of the human hippocampus. *Trends Cogn. Sci.* **17**, 230–240.
- Quax, S.C., D'Asaro, M., and Gerven, M.A.J. van (2019). Adaptive time scales in recurrent neural networks. *BioRxiv*, 800540.
- Rao, R.P., and Ballard, D.H. (1999). Predictive coding in the visual cortex: a functional interpretation of some extra-classical receptive-field effects. *Nat. Neurosci.* **2**, 79–87.
- Reynolds, J.R., Zacks, J.M., and Braver, T.S. (2007). A computational model of event segmentation from perceptual prediction. *Cogn. Sci.* **31**, 613–643.
- Runyan, C.A., Piasini, E., Panzeri, S., and Harvey, C.D. (2017). Distinct time-scales of population coding across cortex. *Nature* **548**, 92–96.
- Schaefer, A., Kong, R., Gordon, E.M., Laumann, T.O., Zuo, X.N., Holmes, A.J., Eickhoff, S.B., and Yeo, B.T.T. (2018). Local-global parcellation of the human cerebral cortex from intrinsic functional connectivity MRI. *Cereb. Cortex* **28**, 3095–3114.
- Schapiro, A.C., Rogers, T.T., Cordova, N.I., Turk-Browne, N.B., and Botvinick, M.M. (2013). Neural representations of events arise from temporal community structure. *Nat. Neurosci.* **16**, 486–492.
- Schmidhuber, J. (1992). Learning complex, extended sequences using the principle of history compression. *Neural Comput.* **4**, 234–242.
- Scott, B.B., Constantinople, C.M., Akrami, A., Hanks, T.D., Brody, C.D., and Tank, D.W. (2017). Fronto-parietal cortical circuits encode accumulated evidence with a diversity of timescales. *Neuron* **95**, 385–398.e5.
- Shankar, K.H., Singh, I., and Howard, M.W. (2016). Neural mechanism to simulate a scale-invariant future. *Neural Comput.* **28**, 2594–2627.
- Shi, J., Wen, H., Zhang, Y., Han, K., and Liu, Z. (2018). Deep recurrent neural network reveals a hierarchy of process memory during dynamic natural vision. *Hum. Brain Mapp.* **39**, 2269–2282.
- Simony, E., Honey, C.J., Chen, J., Lositsky, O., Yeshurun, Y., Wiesel, A., and Hasson, U. (2016). Dynamic reconfiguration of the default mode network during narrative comprehension. *Nat. Commun.* **7**, 12141.
- Spitman, M.M., Seo, H., Lee, D., and Soltani, A. (2020). Multiple timescales of neural dynamics and integration of task-relevant signals across cortex. *BioRxiv*, 2020.02.18.955427.
- Sporns, O., Honey, C.J., and Kötter, R. (2007). Identification and classification of hubs in brain networks. *PLoS ONE* **2**, e1049.
- Stephens, G.J., Honey, C.J., and Hasson, U. (2013). A place for time: the spatiotemporal structure of neural dynamics during natural audition. *J. Neurophysiol.* **110**, 2019–2026.
- Sutton, R.S. (1995). TD models: modeling the world at a mixture of time scales. In *Machine Learning Proceedings 1995 (Elsevier)*, pp. 531–539.
- Townsend, J.T., and Ashby, F.G. (1983). *The Stochastic Modeling of Elementary Psychological Processes* (Cambridge University Press).
- Wacongne, C., Labyt, E., van Wassenhove, V., Bekinschtein, T., Naccache, L., and Dehaene, S. (2011). Evidence for a hierarchy of predictions and prediction errors in human cortex. *Proc. Natl. Acad. Sci. USA* **108**, 20754–20759.
- Wasmuht, D.F., Spaak, E., Buschman, T.J., Miller, E.K., and Stokes, M.G. (2018). Intrinsic neuronal dynamics predict distinct functional roles during working memory. *Nat. Commun.* **9**, 1–13.
- Watanabe, T., Rees, G., and Masuda, N. (2019). Atypical intrinsic neural time-scale in autism. *eLife* **8**, e42256.
- Yeshurun, Y., Nguyen, M., and Hasson, U. (2017). Amplification of local changes along the timescale processing hierarchy. *Proc. Natl. Acad. Sci. USA* **114**, 9475–9480.
- Zacks, J.M., and Tversky, B. (2001). Event structure in perception and conception. *Psychol. Bull.* **127**, 3–21.
- Zhou, J., Benson, N.C., Kay, K.N., and Winawer, J. (2018). Compressive Temporal Summation in Human Visual Cortex. *Journal of Neuroscience* **38**, 691–709.
- Zuo, X., Honey, C.J., Barense, M.D., Crombie, D., Norman, K.A., Hasson, U., and Chen, J. (2020). Temporal integration of narrative information in a hippocampal amnesic patient. *NeuroImage*. <https://doi.org/10.1016/j.neuroimage.2020.116658>.

## STAR★METHODS

### KEY RESOURCES TABLE

REAGENT or RESOURCE	SOURCE	IDENTIFIER
Deposited Data		
Neuroimaging Data	Nastase et al. (2019)	<a href="https://openneuro.org/datasets/ds002345/">https://openneuro.org/datasets/ds002345/</a>
Software and Algorithms		
Python	Python	<a href="https://www.python.org">https://www.python.org</a>
HAT Model	Custom Software	<a href="https://github.com/HLab/ContextConstruction">https://github.com/HLab/ContextConstruction</a>

### LEAD CONTACT AND MATERIALS AVAILABILITY

Further information and requests for resources should be directed to and will be fulfilled by the Lead Contact, Christopher J. Honey ([chris.honey@jhu.edu](mailto:chris.honey@jhu.edu)).

Neuroimaging data and stimuli are available at <https://openneuro.org/datasets/ds002345> (alias: notthefall).

Python model implementations are available at <https://github.com/HLab/ContextConstruction>.

### EXPERIMENTAL MODEL AND SUBJECT DETAILS

#### Subjects

Forty-three subjects (all native English speakers) were recruited from the Princeton community (20 male, 23 female, ages 18-29). Out of the 43 subjects, 21 subjects participated only in the intact condition, 21 subjects participated only in the scramble condition, and one subject participated in both conditions. Nine subjects (all native English speakers) were recruited from the Johns Hopkins community (5 male, 4 female, ages 19-41), and all 9 subjects participated in both intact and scramble conditions. All subjects had normal hearing and provided informed written consent prior to the start of the study in accordance with experimental procedures approved by the Princeton University Institutional Review Board (Princeton data) and the Johns Hopkins Medical Institute Institutional Review Board (Johns Hopkins data). Conditions in which the head motion were  $> 1$  mm or where the signal was corrupted were discarded from the analysis. Overall, 31 subjects participated in the intact condition, and 31 subjects participated in the scramble condition.

#### Acquiring and Preprocessing of Neuroimaging Data

##### Princeton Dataset

Imaging data were acquired from Princeton Neuroscience Institute (Nastase et al.), on a 3T full-body scanner (Siemens Skyra) with a 20-channel head coil using a T2\*-weighted echo planar imaging (EPI) pulse sequence (TR 1500 ms, TE 28 ms, flip angle 64°, whole-brain coverage 27 slices of 4 mm thickness, in-plane resolution 3 by 3 mm, FOV 192 by 192 mm). Preprocessing was performed in FSL, including slice time correction, motion correction, linear detrending, high-pass filtering (140 s cutoff), coregistration and affine transformation of the functional volumes to a template brain (MNI). Functional images were resampled to 3 mm isotropic voxels for all analyses.

##### Johns Hopkins Dataset

Imaging data were acquired on a 3T full-body scanner (Phillips Elition) with a 20-channel head coil using a T2\*-weighted echo planar imaging (EPI) pulse sequence (TR 1500 ms, TE 30 ms, flip angle 70°, whole-brain coverage 28 slices of 3 mm thickness, in-plane resolution 3 by 3 mm, FOV 240 by 205.7 mm). Preprocessing was performed in FSL, including slice time correction, motion correction, linear detrending, high-pass filtering (140 s cutoff), and coregistration and affine transformation of the functional volumes to a template brain (MNI). Functional images were resampled to 3 mm isotropic voxels for all analyses.

### METHOD DETAILS

#### Linear Integrator Models

The linear integrator model was adapted and modified from the classical temporal context model (TCM). TCM successfully accounts for human sequence encoding and retrieval behavior, using the concept of a drifting internal context (Howard and Kahana, 2002). The linear integrator model employs two buffers, each of which is represented as a real-valued vector: the feature buffer which contains the features of items processed in the sequence stream; and the context buffer (CNTX) composed of a “temporal context vector.” A weight matrix  $M^{FT}$ , which is trained by Hebbian learning mechanism, maps stimulus features to their corresponding representation in

the context space; this transformation results in an “input vector,”  $IN$ . At each time step, the temporal context at the next time point  $CNTX(t + 1)$  is updated by adding the mapped input  $IN(t)$  to the prior context  $CNTX(t)$ :

$$CNTX(t + 1) = \rho_i CNTX(t) + \beta_i IN(t) \quad (1)$$

where  $\rho_i$  determines the rate of temporal integration, and we choose  $\rho_i \approx \sqrt{1 - \beta_i^2}$  in order to prevent the  $CNTX$  vector from changing its length.

### Parallel Linear Integrator Model: PLI

In order to simulate a multi-scale temporal integration process without hierarchical information transmission, we built a parallel linear integration model (PLI), in which we set the  $\beta_i$  parameter in Equation 1 to 0.9, 0.7 and 0.5 for Level 1, Level 2 and Level 3 of the model, respectively. Thus, in the PLI model, all levels receive the same input  $IN$ , but the higher levels of the model will preserve more context (via their larger  $\rho$  parameters).

### Hierarchical Linear Integrator Model: HLI

In order to approximate a sequence of processing stages in a cortical hierarchy, we implemented a hierarchical linear integrator (HLI) model in which the output of lower stages serves as the input to the next stage of processing. In particular, we stacked the three linear integrator units (Equation 1), with time constants set just as for the PLI model. However, the input vector  $IN$  for stage  $N+1$  of the model was taken to be equal to the  $CNTX$  vector from stage  $N$ .

### The Signal Gain Model

We implemented a simple signal gain model whose architecture is similar to the PLI model, but where the signal,  $X(t)$ , is unaffected by its previous state. In particular, we set  $\rho_i = 0$  in Equation (1). The signal gain model assumes that (i) scrambling the stimulus decreases the relative magnitude the stimulus representation and (ii) this effect is larger in higher-order brain regions. Thus, to simulate scrambling effects, we decreased the signal-to-noise ratio in the model for higher processing stages or finer scrambling conditions. In particular, we decreased signal-to-noise ratio by increasing the noise amplitude,  $\sigma$ , as follows:

$$X(t) = IN(t) + \epsilon_{layer}(t) \epsilon_{scramble}(t) \quad (2)$$

where  $\epsilon_{layer}(t)$  and  $\epsilon_{scramble}$  are independent random variables, sampled independently at each time step from a Normal distribution with 0 mean and standard deviations  $\sigma_{layer}$  and  $\sigma_{scramble}$ , respectively. Implementing the assumptions of the signal gain model for simulating the context dependence effect (Figure S2), we set  $\sigma_{layer} = 0$  in Layer 1,  $\sigma_{layer} = 0.05$  in Layer 2, and  $\sigma_{layer} = 0.09$  in Layer 3 to simulate hierarchical temporal integration; and we set  $\sigma_{scramble} = 0.1, 0.5$  or  $0.9$  for the paragraph-level, sentence-level, and word-level scrambling conditions.

### Hierarchical Autoencoders in Time: HAT Model

#### Local processing unit: the AT module

Each local processing stage in HAT is an “autoencoder in time” (AT) module. This AT module was adapted from the TRACX2 model for modeling human statistical learning and sequence learning behavior (Mareschal and French, 2017). Each AT module consists of three layers. There is an input layer (consisting of a concatenated input unit,  $IN$ , and a context unit,  $CNTX$ ); there is a hidden layer (HID) which stores the compressed representation of the input layer; and there is an output layer storing the reconstruction of the input layer from the compressed HID representation (Figure S1). During training, the model will learn good internal (i.e., HID) representations of the  $[CNTX, IN]$  pairings that occur frequently. At the end of training, it should be able to accurately reconstruct “chunks” of input-and-context from the compressed (i.e., lower-dimensional) internal representation, HID.

In the AT module, information from the world is presented as a stream of symbols, one symbol at a time. For every time step of the model, the current input symbol,  $S_t$ , from the sensory environment is represented as a 1-by- $N$  one-hot vector, where one scalar value is 1 and all others are  $-1$ . This new input vector is mapped to the  $IN$  bank at each time step. The prior context stored in the model is represented as another 1-by- $N$  vector, which is stored in the  $CNTX$  bank.

Each time-step of the model proceeds as follows (please refer to Figure S1):

- A. For the very first timestep, the model is initialized with two consecutive stimuli ( $S_{t-1}, S_t$ ) in the  $CNTX$  and  $IN$  banks ( $CNTX_1 = S_0, IN_1 = S_1$ ). For all subsequent timesteps, the  $CNTX$  vector is updated according to Equation 7 (below), while  $IN_t = S_t$ .
- B. Activity is propagated forward from the input and context banks (jointly of length 1-by- $2N$ ) to the hidden bank (1-by- $N$ ) via an affine transformation followed by a hyperbolic nonlinearity.

$$HID_{1 \times N} = \tanh([CNTX, IN]_{1 \times 2N} \times V_{2N \times N}) \quad (3)$$

Thus, a compressive transformation is implemented via the mapping from the input and context (1-by- $2N$ ) to the hidden units,  $HID_t$  (1-by- $N$ ). A weight matrix  $V$  (of size  $2N \times N$ ) contains the synaptic weights that transform the input layer to the hidden layer in this compression stage. After the hidden units in the model are updated in this way, another linear-nonlinear transformation is used

to update the output nodes. A second weight matrix,  $W$  (of size  $N \times 2N$ ), is then right-multiplied with the hidden layer vector,  $HID_t$ , generating an output bank that is meant to approximately reconstruct the input bank of the model:

$$[CNTX', IN']_{1 \times 2N} = \tanh(HID_{1 \times N} \times W_{N \times 2N}) \quad (4)$$

**C.** The objective is to make the “reconstruction” in the output banks,  $[CNTX', IN']$ , as similar as possible to the actual input  $[CNTX, IN]$ . Therefore, an auto-associative error  $\Delta$  is generated as the absolute difference of the input and output layer (the difference of the veridical and reconstructed representations):

$$\Delta = |[CNTX', IN'] - [CNTX, IN]| \quad (5)$$

**D.** The “surprise” parameter,  $\alpha$ , is calculated as the maximum value of  $\Delta$ , multiplicatively scaled by a parameter  $k$ :

$$\alpha = \tanh(k \max(\Delta)) \quad (6)$$

Here,  $\alpha$  is taken to indicate the “surprise” or “familiarity” that the model experiences in response to the combination of the current context,  $CNTX$ , and the current input,  $IN$ . When  $k$  is larger, the average amount of surprise (magnitude of  $\alpha$ ) is increased, and  $IN$  makes a larger contribution to the  $CNTX$  variable at the next time step.

The  $CNTX$  bank is updated as a linear mixture of  $IN(t)$  and  $HID(t)$ , weighted by the surprise parameter,  $\alpha$ :

$$CNTX(t+1) = (1-\alpha)HID(t) + \alpha IN(t) \quad (7)$$

If  $\alpha$  is large, the model has not learned a good  $HID$  representation for accurately reconstructing  $IN_t$  and  $CNTX_t$ , and so the  $CNTX_{t+1}$  bank will be overwritten by the input  $IN_t$ . If  $\alpha$  is small, the model has learned a good compressed joint representation,  $HID_t$ , and this compressed representation becomes the context that is used for associating with the next sequential input  $IN_{t+1}$ .

The steps from **A-D** complete one iteration of the model, and the cycle continues with step **A**.

When the model is trained, the transformation matrices (matrix  $V$  mapping from input layer to hidden layer, and matrix  $W$  mapping from hidden to output layer, [Figure S1](#)) are adjusted via backpropagation. The loss function is the norm of the auto-associative error vector  $\Delta$ . The backpropagation weight updates are performed incrementally, one training exemplar at a time. Backpropagation is entirely local to each processing unit (it is not performed end-to-end across the entire network, even when AT units are stacked).

As the model is exposed to the sequential regularities of the input stream, it gradually learns good internal representations of  $[CNTX, IN]$  sequences, and so the auto-associative error gradually decreases. The model can also detect event boundaries in the input sequence: at event boundaries, the model will be unable to generate an accurate compressed representation of  $[CNTX, IN]$ , and will generate a large error  $\alpha$ . This large error will then bias the model to overwrite its prior context (from the old event) with its current input (from the new event).

In summary, the AT module exhibits three important features: (1) prior context is preserved in the  $CNTX$  bank; (2) the updating / overwriting of prior context is gated by an auto-associative error  $\Delta$  which is summarized in the “surprise” parameter,  $\alpha$ ; and (3) the model minimizes its auto-associative error  $\Delta$  by learning the statistical relationships between prior context and new input.

We hypothesize that each stage of processing in the cortical hierarchy exhibits these three functional properties. Therefore, the HAT model is thus composed of a stack of AT modules, each with these functional properties.

### **Stacked AT Modules: Hierarchy of Autoencoders**

We employed a HAT model with three levels ([Figure 5B](#)). Each level is an AT module. The information flow in HAT is globally feedforward with local feedback: each AT module receives recurrent input from its own past state, but there is no backward information flow from AT module  $i+1$  to AT module  $i$ .

Information processing in the HAT architecture possess two key features: first, the context update depends on a local timescale and is gated by surprise; second, the information flow between levels is gated by surprise.

#### **Context update via timescale and surprise:**

[Figure 5C](#) illustrates the structure of each AT module in HAT. As described above, the AT module transforms the input and context  $[CNTX, IN]$  into a compressed internal representation,  $HID$ , and the model then attempts to reconstruct the  $[CNTX, IN]$  pairing from this lower-dimensional internal representation. The local context in each level unit is updated by a combination of  $HID$  and  $IN$ , modulated by a level-specific time constant  $\tau$  and local surprise  $\alpha$ , respectively ([Figure 5C](#)). If  $\tau$  is larger than  $\alpha$ , the model tends to preserve more context from  $HID$ ; if  $\alpha$  is larger than  $\tau$ , the model tends to overwrite the context using the current input  $IN$ , as the equation illustrates:

$$CNTX_i(t+1) = \frac{\tau_i}{\tau_i + \alpha_i} \times HID_i(t) + \frac{\alpha_i}{\tau_i + \alpha_i} \times IN_i(t) \quad (8)$$

Note that in the full HAT model implementation reported in the main text, we employed [Equation 8](#) rather than the simpler [Equation 7](#) which describes a single AT module.

To capture the assumption that higher-level regions process information over longer timescales while lower-level regions process information over shorter timescales, we set  $\tau$  equal to 0.8 for the top level, 0.5 for the middle level and 0.2 for the bottom level of the 3-level HAT model. Thus, relative to the lower levels of the model, the CNTX variable in higher levels of the model will preserve more information about the context in prior timesteps. Of course, in addition to this fixed parameter  $\tau$  which determines how much context is typically preserved in each level, the context updating is also influenced by the surprise parameter,  $\alpha$ , which can transiently increase the influence of the input  $IN$  the update of the CNTX variables.

#### **Information flow in HAT is gated by surprise**

We designed the feedforward information flow in HAT based on the notion that temporal integration is a distributed process, assuming that higher-level circuit perform a similar operation to lower-level circuits (i.e., linking input to prior context) but the higher levels may learn to associate chunks instead of single elements in the sequence. Our goal was that, for a multi-level compound like the word *airplane*, the first level of the model might learn to chunk the phonemes within *air* and *plane*, and the second level might learn to chunk *air* and *plane* to represent the larger word *airplane*. Thus, the input to the higher levels of the HAT model should be the compressed (chunked) representations from the lower levels. However, this process should also be modulated by surprise, as higher levels should only accept “successful” chunks from the layer below.

Therefore, the input to the higher levels of HAT is a linear mixture of HID and IN from the level below, modulated by the surprise  $\alpha$ :

$$IN_{i+1}(t) = (1 - \alpha_i) \times HID_i(t) + \alpha_i \times IN_i(t) \quad (9)$$

If the lower-level unit detects a large surprise (if  $\alpha$  is near 1), more of the lower-level’s input would be passed on as input to the upper level. On the other hand, if the lower-level unit detects small surprise (if  $\alpha$  is near 0), then the “temporal chunk” representation from the lower level would be transmitted as input to the upper level (Figure 5D).

#### **Nonlinearity**

In the HAT model, the representation of a word is a nonlinear combination of the letters, which depends on those letters having been seen before in similar sequences. This is in contrast to the HLI model, where the representation is simply an exponentially weighted sum of each item; the relationship of new input and prior context (e.g., whether they are related or unrelated) does not affect the magnitude or form of the context update in HLI.

### **HAT variants**

#### **Parallel AT model**

To examine whether a hierarchical stage-by-stage processing architecture is required to reproduce the empirical phenomena reported here, we implemented a Parallel AT (PAT) model which consists of three AT units with different  $\tau$  parameters (i.e., 0, 0.4 and 0.8 for level 1, 2 and 3, analogous to the hierarchical models). In contrast to HAT, each AT unit in the PAT model directly receives the same sequence of inputs from the environment. The inputs are processed in parallel, without any interaction between the AT units.

#### **HAT variants with limited gating**

To examine whether context gating is a necessary mechanism for the HAT model to be able to reproduce the empirical phenomena of hierarchical temporal integration, we generated a set of HAT models with variations in their gating mechanisms. Specifically, we turned off the surprise-modulated context gating mechanism, either locally (i.e., the context gating within each AT module) or globally (i.e., the gating of transmission between levels of the model), or we turned off all gating effects.

#### **HAT-Local Gating: HAT-LG**

HAT-LG is a HAT model with only local gating (within each AT module) but no transmission gating mechanism (between AT modules). Thus, the input to the higher levels of the model is simply a copy of the HID from the lower level, regardless of the  $\alpha$  parameter (as in Equation 10).

$$IN_{i+1}(t) = HID_i(t) \quad (10)$$

However, the within-level CNTX update is still gated by surprise (Equation 8).

#### **HAT-Transmission Gating: HAT-TG**

HAT-TG is a HAT model with only transmission gating but no local gating mechanism. That is, the local context is updated with a fixed influence of the input, which depends only on the level-specific  $\tau$  (Equation 2) without the modulation of surprise  $\alpha$ .

$$CNTX_i(t + 1) = \tau_i \times HID_i(t) + (1 - \tau_i) \times IN_i(t) \quad (11)$$

However, the between-level transmission is still gated by surprise  $\alpha$  from level below, as in Equation 9.

#### **HAT-No Gating: HAT-NG**

HAT-No Gating or HAT-NG, is a HAT model with neither local nor transmission gating mechanism. There is no surprise-modulated gating mechanism: instead, the local context is updated with a fixed influence from the input, which depends only on the level-specific  $\tau$  (Equation 11). Moreover, there is no transmission gating in this model: the input of the upper level is a copy of the HID vector from the lower level, as described in Equation 10).

## Model Simulations and Predictions

### Simulations of Hierarchical Context Dependence

To test for the phenomenon of hierarchical context dependence in each model (Figure 1D), we employed a strategy analogous to the original human experiments. We presented the model with intact and scrambled versions of a time-varying stream of input. We then measured the context effects by comparing the model responses (internal representations) of the same input preceded by different contexts.

As described in the main text, for a model to account for the hierarchy of context dependence it should capture two key phenomena:

- (P1) lower processing stages of the model should be insensitive to context change (analogous to sensory cortical regions, Figure 1D, left bars);
- (P2) increasingly higher processing stages of the model should be increasingly sensitive to temporal context further in the past (analogous to higher stages of cortical processing, Figure 1D, right bars).

We trained and tested six different models, including the signal gain model, the parallel linear integrator model (PLI), the HLI model, the parallel autoencoders in time model (PAT), as well as the HAT model, and the no-gating variant of the HAT model. In addition, we tested (for each model) whether the context dependence effect was selective for previously trained sequences. In other words, we measured the “learning effect” (Table S1, see below).

### Model Training Procedure

To examine whether each of our models exhibit a hierarchy of context dependence, we simulated an approximation of the experimental paradigm in Lerner et al. (2011). We trained the models with a 30-element long “intact” sequence. The intact sequence was presented 600 times. Each element of the input was encoded as a one-hot vector of length 30. We also added uniformly distributed noise to each scalar value of each input sequence. The noise samples were independently drawn from a uniform distribution on [-0.3, 0.3]. The purpose of the noise was to improve the model’s generalizability, and to approximate the fact that real-world sequence learning occurs in the presence of noise. To prevent the model from learning a spurious relationship between the end of the intact sequence and the beginning of the next presentation of the intact sequence, we added “random filler” sequences (length = 5 symbols) between intact segments. Each of the random filler symbols was an independently generated random vector, with elements uniformly distributed in the range [-1, 1] for the HAT model and its variants, and in the range [0,1] for other models. (Figure S2A, depicted as an ‘x’ between intact segments).

### Testing Models for Context Dependence

After training, the weights in each model were fixed; no further weight change was allowed during test. During testing, we then compared the models’ representations of intact and scrambled sequences. The three scrambled sequences were designed to preserve the intact structure at three different scales: the long-scale (6 element subsequences were preserved), medium-scale (3 element subsequences were preserved) and fine-scale (2 element subsequences were preserved). Each testing ensemble (e.g., “medium scale scramble”) was composed of 10 “test sequences.” Each test sequence was a length-30 sequence which was a randomly scrambled version of the intact sequence. All test sequences within an ensemble were scrambled at the same scale, but with different permutations. Therefore, each test sequence exhibited preserved structure on the relevant scale. As during training, fillers were again inserted between each of the 10 sequences that composed a testing ensemble (Figure S2A, the ‘x’ between the length-30 test sequences). We then defined the “context dependence” (CD) effect as the difference in intact-scramble correlation across the long-scramble and short-scramble conditions:  $CD = \text{corr}(\text{intact}, \text{LSS}) - \text{corr}(\text{intact}, \text{FSS})$  (see Figure S2).

### Testing the Effect of Learning on Context Dependence

To assess whether models captured the temporal structure of the intact sequences due to sequence-specific learning (rather than due to an intrinsic ability to maintain prior context of any kind of sequence), we additionally trained models with random sequences, that were generated by shuffling the intact structured sequences. We then tested these shuffle-trained models with the same (non-random) testing sequences that were used to test the normal structure-trained models. In this way, we could compare the CD effects for the models trained with structured sequences against the CD effect for models trained with randomly shuffled sequences (Figure S5C). We defined the “learning effect” as the difference in CD values between a model trained with structured sequences and the same model trained with shuffled sequences.

### Simulations of Context Construction and Forgetting

We set out to model the context construction results (Figures 2 and 3) using the signal gain model, the linear integrator models and the HAT model and its variants. The training sequences and procedure were the same as for modeling of the Lerner et al. (2011) data. For testing, we only simulated the models with the intact and the paragraph-level scrambled sequences, as we took these levels to correspond to the intact and scramble conditions in the empirical data.

Timescales of alignment and separation were analyzed in the model in an analogous manner to how they were assessed in the empirical data. For clarity, we introduce notation that discriminates the cross-group similarity measure, rSI, as it is used in the alignment and separation analyses. Specifically, we employ  $rSI_{\text{CONSTRUCT}} = rSI_{\text{DE:CE}}$  for the rSI in the context alignment (“construction”) analysis, and  $rSI_{\text{FORGET}} = rSI_{\text{CD:CE}}$  for the rSI in the context separation (“forgetting”) analysis. The context

alignment curve,  $rSI_{DE:CE}$ , was estimated by computing ISPC on the internal representations of each model. Internal representations were measured when the same six-element segments were presented as input, preceded by different segments in the intact and scramble group. Similarly, for the separation curve,  $rSI_{CD:CE}$ , the correlations were measured in the model simulation by performing ISPC on the hidden representations across two different “groups” of model runs.

To simulate different “participants,” we added noise to the inputs of each model, so that there would be some variation across runs in the generated responses. In particular, for the HAT model we added independent random sample from a Normal distribution  $\sim \mathcal{N}(0, 0.5)$  and for the HLI model we added independent random noise  $\sim \mathcal{N}(0, 2)$  (the HLI model noise was larger, in order to generate more variance between “subjects” and better approximate the empirical data pattern). These noise samples were added independently to each element of the input vector on each timestep. In this way, by running 200 simulations, each with unique noise structure, we generated 100 simulated “subjects” for the intact group and 100 simulated “subjects” for the scrambled group.

Each model run was treated in the same way as the neural response of a single participant. Thus, we measured the responses across two groups of model runs, where responses were correlated across different segments (e.g., segment D in Group 1 and segment E in Group 2) which were preceded by the same segment (e.g., segment C was the preceding segment in both Group 1 and Group 2).

To compare the patterns of model predictions against empirical data, we also approximated the effect of “hemodynamics” in our model, by convolving the time course of each model’s internal representation with a temporal smoothing function. This convolution was performed only on the model output, and did not affect the internal dynamics of the simulation. The temporal smoothing function in the model consisted of two gamma functions to approximate the hemodynamic response (HRF). The probability density function of the gamma function is:

$$f(x, a) = \frac{x^{a-1} \exp(-x)}{\Gamma(a)}$$

Here we set  $a = 2.5$  for one gamma function to set the peak value, and  $a = 2$  for the other gamma function for the undershoot value of our HRF.

### Analysis of Linear Integrators

We analytically confirmed that the “alignment time” and the “separation time” of a linear integrator model are closely related. In particular, in limiting cases of simple linear integrators, the alignment time and separation are expected to be identical.

We consider two integrators, A and B, each of which is treated as a model of one participant. We will measure the correlation of the state of these integrators as a function of time.

At each time,  $t$ , the state of each integrator is an  $n$ -dimensional vector:

$$A_i(t) = \text{scalar value of voxel } i \text{ in participant } A \text{ at time } t$$

$$B_i(t) = \text{scalar value of voxel } i \text{ in participant } B \text{ at time } t$$

Then we can define the vector of initial states of each integrator:

$$\mathbf{A}(0) = \text{initial state of vector } \mathbf{A}$$

$$\mathbf{B}(0) = \text{initial state of vector } \mathbf{B}$$

and we can define the vector of time-varying input that each integrator receives:

$$\mathbf{I}_A(t) = \text{input to } \mathbf{A} \text{ at time } t$$

$$\mathbf{I}_B(t) = \text{input to } \mathbf{B} \text{ at time } t$$

The alignment time is the time for two integrators to produce a similar response after receiving a series of identical inputs. Thus, to measure the alignment time, we assume that  $\mathbf{A}(0)$  and  $\mathbf{B}(0)$  are random initial starting points (each  $A_i(0) \sim N(0, 1)$ , each  $B_i(0) \sim N(0, 1)$ ) but the input is identical, so that  $\mathbf{I}_A(t) = \mathbf{I}_B(t)$  for all  $t$ . Under these conditions, we write  $\mathbf{A}(t) = \mathbf{A}_{align}(t)$ ,  $\mathbf{B}(t) = \mathbf{B}_{align}(t)$ , and we define the “alignment similarity” using the Pearson correlation:

$$r_{align}(t) = \text{corr}(\mathbf{A}_{align}(t), \mathbf{B}_{align}(t))$$

Suppose the alignment time is the smallest  $t$  for which  $r_{ALIGN}(t) > K$  where  $0 < K < 1$  is an arbitrary threshold.

The separation time is the time for two integrators to produce a dissimilar response after receiving independent input. Thus, to measure the separation time, we assume that  $\mathbf{A}(0) = \mathbf{B}(0)$  while the inputs,  $\mathbf{I}_A(t)$  and  $\mathbf{I}_B(t)$ , are statistically independent draws

from  $N(0,1)$ . Under these conditions, we write  $\mathbf{A}(t) = \mathbf{A}_{sep}(t)$ ,  $\mathbf{B}(t) = \mathbf{B}_{sep}(t)$ , and we now define the separation similarity using the Pearson correlation:

$$r_{sep}(t) = \text{corr}(\mathbf{A}_{sep}(t), \mathbf{B}_{sep}(t)) < 1 - K$$

Suppose that the separation time is the smallest  $t$  for which  $r_{SEP}(t) < 1 - K$  where  $0 < K < 1$  is the same threshold as chosen for the alignment time.

To show that alignment times and separation times are tightly related, we will show that

$$r_{align}(t) + r_{sep}(t) = 1$$

so that  $r_{align}$  must increase at the same rate as  $r_{sep}$  decreases. Thus, for any choice of threshold,  $K$ , the time to align and the time to separate are equal.

For the update of our discrete-time linear integrator, we take:

$$A_i(t+1) = \rho A_i(t) + \lambda I_{A,i}(t)$$

where  $\lambda = \sqrt{1 - \rho^2}$ .

By definition,

$$A_i(1) = \rho A_i(0) + \lambda I_{A,i}(0)$$

and

$$A_i(2) = \rho A_i(1) + \lambda I_{A,i}(1) = \rho[\rho A_i(0) + \lambda I_{A,i}(0)] + \lambda I_{A,i}(1) = \rho^2 A_i(0) + \sum_{m=0}^1 \rho^{1-m} \lambda I_{A,i}(m)$$

We can iterate this equation to derive the form of  $A_i(t)$ :

$$A_i(t) = \rho^t A_i(0) + \sum_{m=0}^{t-1} \rho^{t-1-m} \lambda I_{A,i}(m)$$

and similarly

$$B_i(t) = \rho^t B_i(0) + \sum_{m=0}^{t-1} \rho^{t-1-m} \lambda I_{B,i}(m)$$

We assume that each of the scalar values within the inputs,  $I_{A,i}$  and  $I_{B,i}$ , are independent draws from a Normal distribution with zero mean and unit variance. In conjunction with the choice of  $\lambda = \sqrt{1 - \rho^2}$ , which scales the relative amplitudes of prior states of the integrator and its new input, this guarantees that  $E[A_i(t)] = E[B_i(t)] = 0$  and  $\text{VAR}[A_i(t)] = \text{VAR}[B_i(t)] = 1$ .

Now suppose we consider the expression for the sample Pearson product-moment correlation between  $\mathbf{A}(t)$  and  $\mathbf{B}(t)$ . This is a correlation computed across voxels (i.e., the vector  $\mathbf{A}(t)$  correlated with the vector  $\mathbf{B}(t)$ ). If we assume that each vector is composed of  $n$  voxels, then the correlation takes the following form:

$$r_{AB}(t) = \text{corr}(\mathbf{A}(t), \mathbf{B}(t)) = \frac{\sum_{i=1}^n A_i(t) B_i(t) - n \mu_{A(t)} \mu_{B(t)}}{(n-1) s_{A(t)} s_{B(t)}}$$

where  $\mu_{A(t)}$  and  $\mu_{B(t)}$  are the sample means of the vectors, and  $s_{A(t)}$  and  $s_{B(t)}$  are their sample standard deviations.

By construction, the individual linear integrator units maintain a mean value of zero, and so  $\mu_{A(t)}, \mu_{B(t)} \rightarrow 0$  as  $n \rightarrow \infty$ . Moreover, because of the choice  $\lambda = \sqrt{1 - \rho^2}$ , which preserves the variance of the individual elements of the vector, the sample standard deviations,  $s_{A(t)}$  and  $s_{B(t)}$  are approximately constant over time.

Therefore, the variation in  $r_{AB}$  over time arises from changes in the inner product of the vectors describing each integrator:

$$\begin{aligned} \sum_{i=1}^n A_i(t) B_i(t) &= \sum_{i=1}^n \left[ \rho^t A_i(0) + \sum_{m=0}^{t-1} \rho^{t-1-m} \lambda I_{A,i}(m) \right] \left[ \rho^t B_i(0) + \sum_{m=0}^{t-1} \rho^{t-1-m} \lambda I_{B,i}(m) \right] \\ &= \sum_{i=1}^n \left[ \rho^t A_i(0) \rho^t B_i(0) + \sum_{m=0}^{t-1} \rho^{t-1-m} \lambda I_{A,i}(m) \rho^t B_i(0) + \sum_{m=0}^{t-1} \rho^{t-1-m} \lambda I_{B,i}(m) \rho^t A_i(0) + \sum_{m=0}^{t-1} \rho^{t-1-m} \lambda I_{B,i}(m) \sum_{m=0}^{t-1} \rho^{t-1-m} \lambda I_{A,i}(m) \right] \\ &\cong \sum_{i=1}^n \left[ \rho^{2t} A_i(0) B_i(0) + \sum_{m=0}^{t-1} \rho^{t-1-m} \lambda I_{B,i}(m) \sum_{m=0}^{t-1} \rho^{t-1-m} \lambda I_{A,i}(m) \right] \end{aligned}$$

This last simplification occurs because the input to the integrators ( $\mathbf{I}_A$  and  $\mathbf{I}_B$ ) are zero-mean vectors that are statistically independent of the initial states ( $\mathbf{A}(0)$  and  $\mathbf{B}(0)$ ); thus the cross-terms that multiply these factors have an expectation of zero, and their contribution to  $r_{AB}$  will tend to zero as  $n \rightarrow \infty$ .

Now, if we consider the formula for  $\sum_{i=1}^n A_i(t)B_i(t)$  above, the first term is a sum over products of the initial states ( $\mathbf{A}(0)$  and  $\mathbf{B}(0)$ ) of the two integrators, while the second term is a sum over products of the inputs to the integrators ( $\mathbf{I}_A$  and  $\mathbf{I}_B$ ). Thus, the variation in the correlation over time can be decomposed into two terms: one term is a contribution from the decaying memory of the initial conditions ( $\mathbf{A}(0)$  and  $\mathbf{B}(0)$ ) while the other term is the contribution from the correlation in the input ( $\mathbf{I}_A$  and  $\mathbf{I}_B$ ) to each linear integrator.

Finally, we can show that the quantity  $r_{align}(t)$  measures the time-varying contribution from shared input, while the quantity  $r_{sep}(t)$  measures the time-varying contribution from the shared initial conditions.

Recall that when we are measuring  $r_{align}(t)$ , we assume that initial states of the two integrators are statistically independent but the inputs are identical. In this case  $E[(\rho^t \mathbf{A}_i(0) \rho^t \mathbf{B}_i(0))] = 0$ , so that:

$$r_{align}(t) \cong \sum_{i=1}^n \left[ \sum_{m=0}^{t-1} \rho^{t-1-m} \lambda_{B,i}(m) \sum_{m=0}^{t-1} \rho^{t-m} \lambda_{A,i}(m) \right] / K$$

where  $K = (n-1)s_{A(t)}s_{B(t)}$  summarizes the length of the vector and the sample standard deviations, which are essentially constant over time and invariant to the initial conditions.

On the other hand, recall that when we are measuring  $r_{SEP}(t)$ , the initial states of the two integrators are identical, but their inputs are statistically independent. In this case,  $E[\sum_{m=1}^t \rho^{t-m} \lambda_{B,i}(m) \sum_{m=1}^t \rho^{t-m} \lambda_{A,i}(m)] = 0$ , so that

$$r_{sep}(t) \cong \sum_{i=1}^n \rho^{2t} A_i(0) B_i(0) / K$$

where again  $K = (n-1)s_{A(t)}s_{B(t)}$ .

Now suppose we have two linear integrators, and we set them to an identical initial state, and we provide them with identical input. In this case, both the initial state and the input are identical, and thus the correlation of the states of these two linear integrators will remain  $r_{identical}(t) = 1$  for all values of  $t$ . But recall that we have shown that the correlation between the states of two linear integrators at time  $t$ , can be expressed as a sum of two values: the correlation that would have been measured if they had *independent initial conditions* (and identical input) and the correlation that would have been measured if they had *identical initial conditions* (and independent input). Thus, we can decompose the “identical” correlation into these two parts, writing:

$$r_{identical}(t) = r_{align}(t) + r_{sep}(t) = 1$$

This identity implies that a linear integrator that generates a rapidly increasing alignment (with a short alignment time) must equally generate a rapidly decreasing separation (with an equally short separation time).

### Empirical Measurements of Context Dependence Temporal Alignment of Neuroimaging Data

We time-shifted the neural response in each participant so as to minimize inter-subject variation in the hemodynamic response (Handwerker et al., 2004). First, we upsampled all BOLD time courses to a 50 Hz timebase. Second, we aligned the neural response time courses across subjects by shifting each subject to maximize the temporal cross-correlation with the mean time course of all other subjects within the A1 region. This shifting process was performed for each subject, iterating until no further shifting occurred. Having mitigated hemodynamic differences in this way, it was then necessary to align all participants to the timebase of the auditory narrative stimulus. A reference time course was generated by convolving the acoustic envelope of the auditory stimulus with a hemodynamic response function. The mean (across subjects) response time course in A1 was then shifted to maximize the correlation with this stimulus reference time course. These operations were performed separately for data from the intact condition and the scramble condition. Finally, we confirmed that the procedure was accurate by showing that the unscrambling procedure was accurate within A1. First, we checked that the intact and scrambled data exhibited the same ramping BOLD time-course in A1, locked to the onset of each sentence within each stimulus. Second, we confirmed that the unscrambled data (dependent on accurate segment onset timing) correlated with the auditory amplitude of the intact stimulus:  $r(\text{intact neural response in A1, intact audio stimulus}) = 0.53$ ;  $r(\text{unscrambled neural response in A1, intact audio stimulus}) = 0.50$ .

We next partitioned the neural responses into distinct segments, based on the segment onset timing within the intact stimulus and scrambled stimulus, and unscrambled the data based on which segments corresponded. Following this permutation, we then evaluated rSI in the primary auditory cortex (A1) and the right temporal parietal junction (rTPJ) to ensure that the unscrambling procedure was successful.

### Inter-subject pattern correlation (ISPC)

The ISPC analysis quantifies the similarity of spatial patterns of neural responses at a moment in time. We quantify the similarity by correlating the pattern of voxel activation at each time point (Figure 2A). Similar to the inter-subject correlation (ISC) analysis which provides a measure of the temporal reliability of the responses to complex stimuli (Hasson et al., 2004), the ISPC analysis provides a measure of the spatial reliability of the response to the stimuli at each time point (see also Zuo et al., 2020). The ISPC method differs

from conventional fMRI data analysis methods in that it circumvents the need to specify a model for the neuronal processes in any given brain region during story listening. Instead, the ISPC method uses one subject's neural responses to a stimulus as a model to predict the neural responses within other subjects.

Using ISPC, we quantified the changes in the neural responses over time within each segment of the auditory stimulus. We computed similarity within the group of subjects listening to the intact story (the intact condition, rII), similarity within the group listening to the scrambled story (the scramble condition, rSS), and similarity across the intact and scrambled groups (rSI) (Figure 2B). The rII and rSS analyses provide an indication of how reliably a given region is responding to the stimulus (Intact or Scrambled) at a particular moment. Conversely, the rSI analysis across the two groups indicates the similarity across two groups, which may be experiencing the same input (but different contexts) or experiencing different input (but with the same prior context). For example, the main analysis (Figure 2C) examines the neural similarity across intact and scrambled groups when subjects process the same segments preceded by different contexts: we correlated responses to segment E, which was preceded by segment D in the intact group but preceded by segment C in the scrambled group). That is, when the context is disrupted in the scramble group, we measure how subjects re-construct the temporal context in order to align with the intact group.

The pattern-correlation method used here provides several practical advantages for measuring integration timescales. First, we showed that it can be used to measure timescales of context forgetting in addition to context construction. Second, the method is efficient: if reference data exists for the responses to the intact stimulus, then an rSI curve can be computed in a single participant using one presentation of one scrambled stimulus. Third, the rSI curve provides a profile of how context influence varies over time. We focused on alignment times in this study, but future studies could use the asymptote and slope of the rSI curve to constrain quantitative models of temporal integration.

### Measuring similarity within and between groups

To calculate rII, we segmented the neural response according to the segments used to make the scrambled stimuli. For each segment, we analyzed the neural response of the first 16 s following segment onset. We performed ISPC by correlating the neural response pattern of one subject in the intact group to the average neural responses of the remaining subjects in the intact group for each time point. This calculation of spatial patterns was performed separately for each time point in each segment. We generated an ISPC time course within each segment for each subject. The rII was calculated by averaging the ISPC time course across all segments and subjects. The rSS was calculated using the same method, within the scramble group. To calculate rSI, for each long segment, we performed ISPC by correlating the neural response pattern of one subject in the scramble group to the average neural response of all subjects in the intact group. The rSI time-course was calculated by averaging the ISPC time-course across all segments and all subjects.

## QUANTIFICATION AND STATISTICAL ANALYSIS

We used a combination of resampling methods and parametric tests to statistically evaluate all empirical and modeling results, as described below under each heading.

### Quantifying context dependence in models

We measured the similarity of the representations generated by different levels of the model as a function of the amount of shared context. To quantify similarity, we correlated the hidden representation that was generated when the models were processing the intact and the scrambled sequences (Figure S2A). Specifically, we correlated the hidden representations of the last elements of the subsequences (e.g., the “r” in “qr”) in each scrambled sequence with the hidden representations of the same elements (the “r” in “qr”) in the intact sequences (see red symbols in Figure S2A). In this way, we measured how the representation of the identical stimulus was altered as a function of the context change.

We then defined the “context dependence” (CD) effect as the difference in intact-scramble correlation across the long-scramble and short-scramble conditions:  $CD = \text{corr}(\text{intact}, \text{LSS}) - \text{corr}(\text{intact}, \text{FSS})$  (see Figure S2). To compare the CD in two models, we computed the distribution of CD values for each network and computed: (i) a parametric t test of the difference in means and (ii) Cohen's *d* to quantify the separation of the distributions.

Training the HAT model on shuffled sequences produced a large and highly statistically significant decrease in sensitivity to temporal context. Comparing the original HAT model against the shuffle-trained variant, we obtained a large and highly statistically significant difference in context dependence: mean CD original = 0.50, mean CD shuffle-trained = 0.10; Cohen's *d* = 5.42;  $t(98) = 27.1$ ,  $p < 0.001$ . The results for other models are shown in Figure S5C.

### Validating neural response reliability

To examine whether there is a hierarchy of context construction in the cerebral cortex, we conducted the ISPC analysis for 400 ROIs across the whole brain, based on the parcellation of the cerebral cortex provided by (Schaefer et al., 2018). To determine the ROIs that showed reliable responses when people were processing the naturalistic narratives, we first identified brain regions that responded somewhat reliably to both the intact and scrambled stimuli. In particular, we chose an arbitrary threshold of  $rSS = 0.06$  which produced a set of ROIs which are visually similar to the set of narrative-responsive regions reported by (Lerner et al., 2011).

We further validated the threshold by conducting a permutation test of the rII in primary auditory cortex, in which we compared the true rII with the “shuffled rII” calculated after shuffling the order of the segments. First, we generated 10,000 shuffled orders of the segments. For each of these shuffled orders, we reordered the neural responses of one subject according to the shuffled order, and calculated the rII between the shuffled neural response of this one subject with the mean neural responses of the rest of the subjects in the intact group (For the other subjects, the order was preserved). We repeated this procedure to all the 31 subjects in the intact group using the same 10,000 shuffled orders, and calculated the average rII for each shuffled order, generating a null distribution of the rII. We found that 0.06 is significantly higher than the null distribution ( $p < 0.0001$ , Figure S3A), confirming that this is a valid threshold for determining ROIs showing reliable responses when people are processing naturalistic stimuli.

Using this validation criterion, we identified 83 ROIs out of 400 ROIs for further analyses. The raw curves of rII and rSS showed that the 83 ROIs showed reliable responses from the beginning to the end of the segments (Figure 2E), further indicating that  $rSS = 0.06$  is a valid threshold to identify ROIs which respond reliably when people processed the intact and the scrambled stimuli.

### Quantifying alignment time

To quantify the alignment time as an index for context construction of different regions, we fit the  $rSI_{DE:CE}$  curves with the logistic function

$$y = \frac{a}{1 + e^{-b(t-c)}} + d$$

by using least-square regression to minimize error. Here,  $y$  is the dependent variable which is the rSI value and  $t$  is the time in seconds since the segment onset. The parameter  $a$  is the curve’s maximum value,  $b$  is the steepness of the curve,  $c$  is the time when the logistic curve reaches its half maximum value, and  $d$  is an offset term to adjust the initial value of the curve. Here we used the parameter  $c$  as the alignment time measurement for each ROI. Among the 83 ROIs which exhibited reliable responses to the scrambled stimuli, 4 ROIs were excluded because the logistic fitting procedure did not reliably converge; the rSI curves for these ROIs are shown in (Figure S3B).

We used a cross-validation approach to confirm that the logistic function is a good model for fitting rSI curves and evaluating the alignment time. In particular, we tested whether the logistic model fit (and associated alignment time) in a given ROI will generalize to predict similar values when the same fitting is preserved for that ROI in a separate group of participants. In each of the 100 folds of the cross-validation procedure, we randomly split the data into two subsets of participants ( $N = 15$  and  $N = 16$ ). We then used the training group ( $N = 16$ ) to estimate model parameters and the second half ( $N = 15$ ) as a test group for measuring out-of-sample error. In the in-sample data, we measured (i) the shape of the rSI curve; and (ii) the best-fit parameters for the logistic fit to that curve. We then measured the shape of the rSI curve in the out-of-sample data. In order to compute test error, we measured the mean squared error (MSE) in two ways. First, we computed MSE-data: we measured the error when predicting the out-of-sample rSI curve using the in-sample rSI curve. Second, we computed MSE-logistic: we measured the error when predicting the out-of-sample rSI curve using the logistic fit to the in-sample curve. After averaging MSE-data and MSE-logistic across all folds, we compared MSE-data and MSE-logistic for each ROI (Figure S3C). If the MSE for the logistic fit is comparable to that for the rSI curve itself, then we concluded that the logistic fit accurately captures the shape of the rSI curve in that ROI. As shown in the figure, the logistic model was not only comparable to the in-sample data in predicting the out-of-sample data, it was often even better, producing a more accurate prediction than the in-sample curve. This cross-validation performance suggests that logistic model (which correctly assumes a ramping profile) is a valid model for approximating the rSI curve and quantifying the alignment time of the data. The quality of the logistic model can also be confirmed by visually inspecting the curve fits (Figure S4A).

Having confirmed that logistic curves provide a good overall model fit, we used bootstrapping to estimate the uncertainty in the alignment time estimates derived from the logistic fits. In each ROI, the alignment time was derived from the  $c$  parameter in the logistic equation above. For each of 1,000 bootstrap iterations, we resampled 31 subjects with replacement from the subject pool, and then recomputed the rSI curve, the logistic fit, and the  $c$  parameters. This generated a distribution of 1,000  $c$  values for each ROI. We then excluded ROIs in which fewer than 90% of the bootstrap values were within 3 s of the originally estimated  $c$  parameter. Using this method, we identified and excluded 9 ROIs out of the 79 ROIs. These ROIs were mostly higher-order regions whose ISPC curves had lower values and lower signal-to-noise compared to other ROIs (Figure S3D). Thus, 70 ROIs proceeded to context construction analysis. Finally, the alignment time of the individual ROIs were mapped from MNI space to a cortical space, and visualized on a cortical surface map using Workbench Viewer (<https://www.humanconnectome.org/software/connectome-workbench>).

### Quantifying separation time

To test the predictions of the HAT and HLI models regarding context forgetting, we performed another ISPC analysis. We operationalized context forgetting by measuring the separation rate of neural dynamics initialized from a common context. In particular, we examined the similarity of neural responses over time across two groups of “subjects” (i.e., model simulations) processing the different segments preceded by the same context. For example, in the  $rSI_{FORGET} (= rSI_{CD:CE})$  analysis, we correlated the responses between segment D in the intact group and segment E in the scramble group, when both were preceded by segment C (Figure 4B). The procedure for calculating procedure of  $rSI_{FORGET} (= rSI_{CD:CE})$  was directly analogous to the calculation of  $rSI_{CONSTRUCT}$  (as illustrated in Figure 2) except that we paired non-matching segments with matching contexts (CD:CE), rather than pairing matching

segments with non-matching contexts (DE:CE). To quantify the rate of context forgetting (i.e., the “separation time”) we used a procedure analogous to that used for measuring alignment times. We fit the  $rSI_{\text{FORGET}}$  curves with the logistic function, and again used the half-maximum value (the  $c$  parameter) as our estimate of separation time. The measurement of ISPC to generate  $rSI_{\text{FORGET}}$  curves was more variable here than for the  $rSI_{\text{CONSTRUCT}}$  analysis, because here we measured the correlation of responses to distinct stimuli, rather than the correlation to identical stimuli. Therefore, it was only possible to successfully fit the  $rSI_{\text{FORGET}}$  curves in 60 of the 70 ROIs from the previous procedure (Figures 4C and 4D), and the ROIs which could not be well-fit were: LH\_SomMotB\_Aud\_8; LH\_TempPar\_3; LH\_TempPar\_4; LH\_TempPar\_6; RH\_SomMotB\_S2\_2; RH\_SomMotB\_S2\_6; RH\_SomMotB\_S2\_10; RH\_ContA\_PFCI\_2; RH\_TempPar\_2; RH\_TempPar\_4.

The rate of separation in the HAT model was more variable across simulation runs than for the HLI model. The variability in the HAT model arises because its performance depends on a nonlinear learning process: the network weight initialization and the specific randomization order for the scrambled stimulus affect the hidden representations that are learned across different runs, and this induces variability in the strength of the gating at sentence boundaries. We plot a representative  $rSI_{\text{FORGET}}$  simulation in Figure 5I, but variability across model runs can be observed in the simulations shown in Figure S5B. Despite this variability, the HAT model was consistently different from the HLI model, which always predicted that regions with slower changes in  $rSI_{\text{CONSTRUCT}}$  would also exhibit slower changes in  $rSI_{\text{FORGET}}$  (Figures 5H and S5B).

### Simulating alignment time and separation time

To obtain a quantitative comparison of model performance and empirical results, we examined the relationship between the alignment time and separation time measured from the ISPC curves generated by each model. For each model we simulated, we computed  $rSI_{\text{CONSTRUCT}}$  and an  $rSI_{\text{FORGET}}$  curves at each level of the model. We then fit these curves with logistic function to get the alignment time and separation time (i.e., the half maximum value of the logistic curve). We repeated this procedure for the PLI, HLI, HAT-NG and HAT model, respectively, until we obtained at least 50 data points for each model (in a small portion of simulations, the curves could not be well-fit by the logistic function, and the simulation was repeated). To summarize the predictions of each model, we plotted the pairs of alignment-separation values across all three levels and all simulations (Figure S5B). Finally, we calculated the Pearson correlation between the alignment time and separation times for each model, as well as associated parametric  $p$  values.

### DATA AND CODE AVAILABILITY

The neuroimaging datasets used and generated during this study are available at Open Neuro (<https://openneuro.org/datasets/ds002345>) under the “notthefall” alias. Python model implementations are available at <https://github.com/HLab/ContextConstruction>.

**Neuron, Volume 106**

**Supplemental Information**

**Constructing and Forgetting Temporal  
Context in the Human Cerebral Cortex**

**Hsiang-Yun Sherry Chien and Christopher J. Honey**

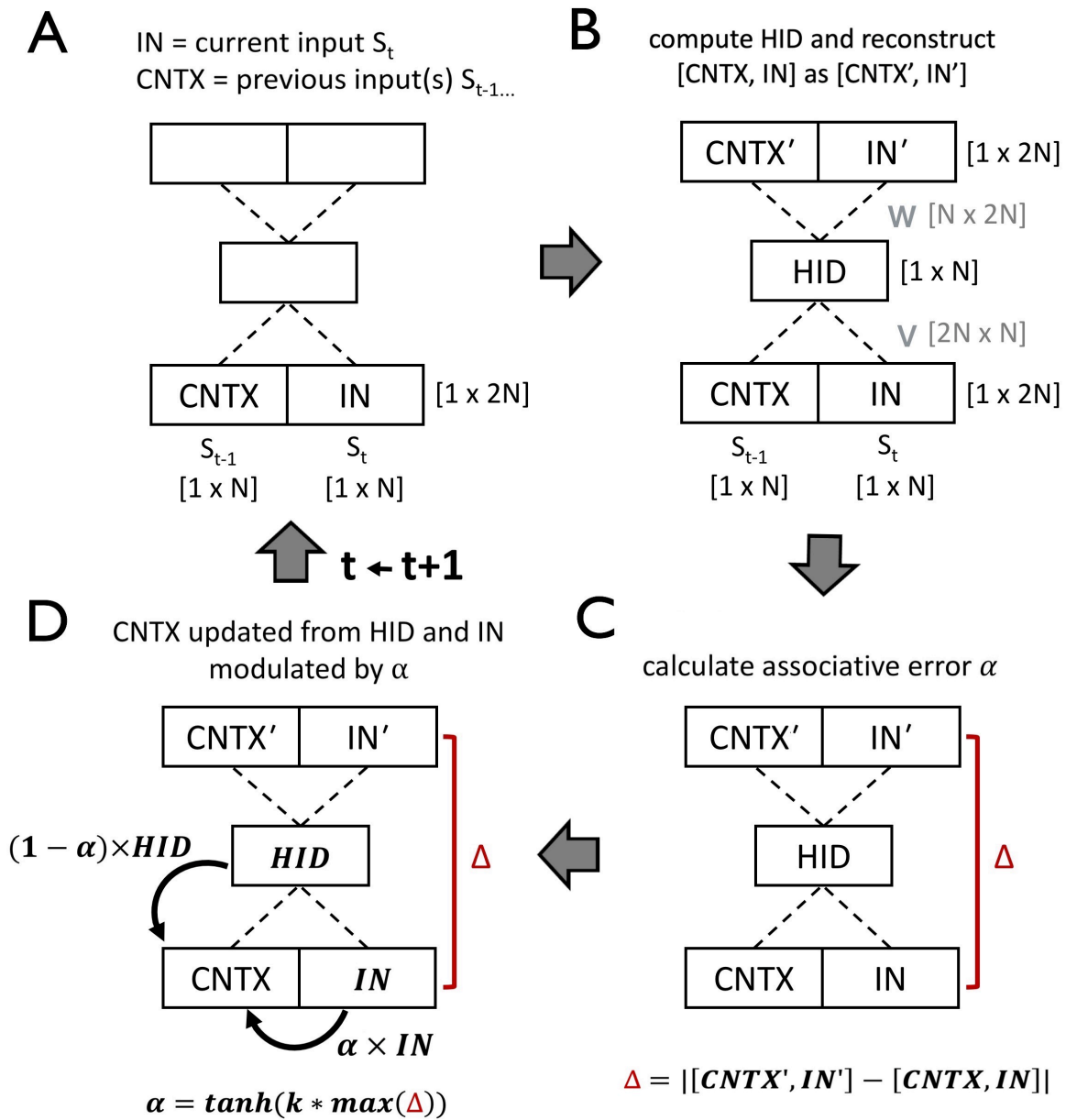


**Figure S1. Architecture and updating of a local autoencoder-in-time (AT) unit. Related to STAR Methods and Figure 5. (A)** At time  $t$ , the input layer of the AT unit is a 1-by- $2N$  vector which contains both the present information  $S_t$  in the IN bank and the past information  $S_{t-1}$  in the CNTX bank. **(B)** The concatenated vector [CNTX, IN] is multiplied by weight matrix  $V$  to form a low-dimensional HID representation (a 1-by- $N$  vector). This HID vector is left-multiplied by a weight matrix  $W$  to generate an output layer [CNTX', IN'] which is the reconstruction of input [CNTX, IN]. **(C)** The reconstruction error,  $\Delta$ , or “surprise”, is calculated as the absolute value of [CNTX', IN']- [CNTX, IN]. **(D)** The gating parameter,  $\alpha$ , is calculated as  $\tanh(k * \max(\Delta))$ . Here, the parameter  $k$  scales how much the contribution of IN to CNTX is increased by surprise. The CNTX vector is updated as a linear mixture of the IN vector and HID vector, with the linear proportions modulated by  $\alpha$  and a level-specific time constant  $\tau$ . After CNTX is updated, the cycle is complete, and the unit is ready to receive input at time  $(t+1)$ . IN = input unit, CNTX = context unit, HID = hidden state unit.

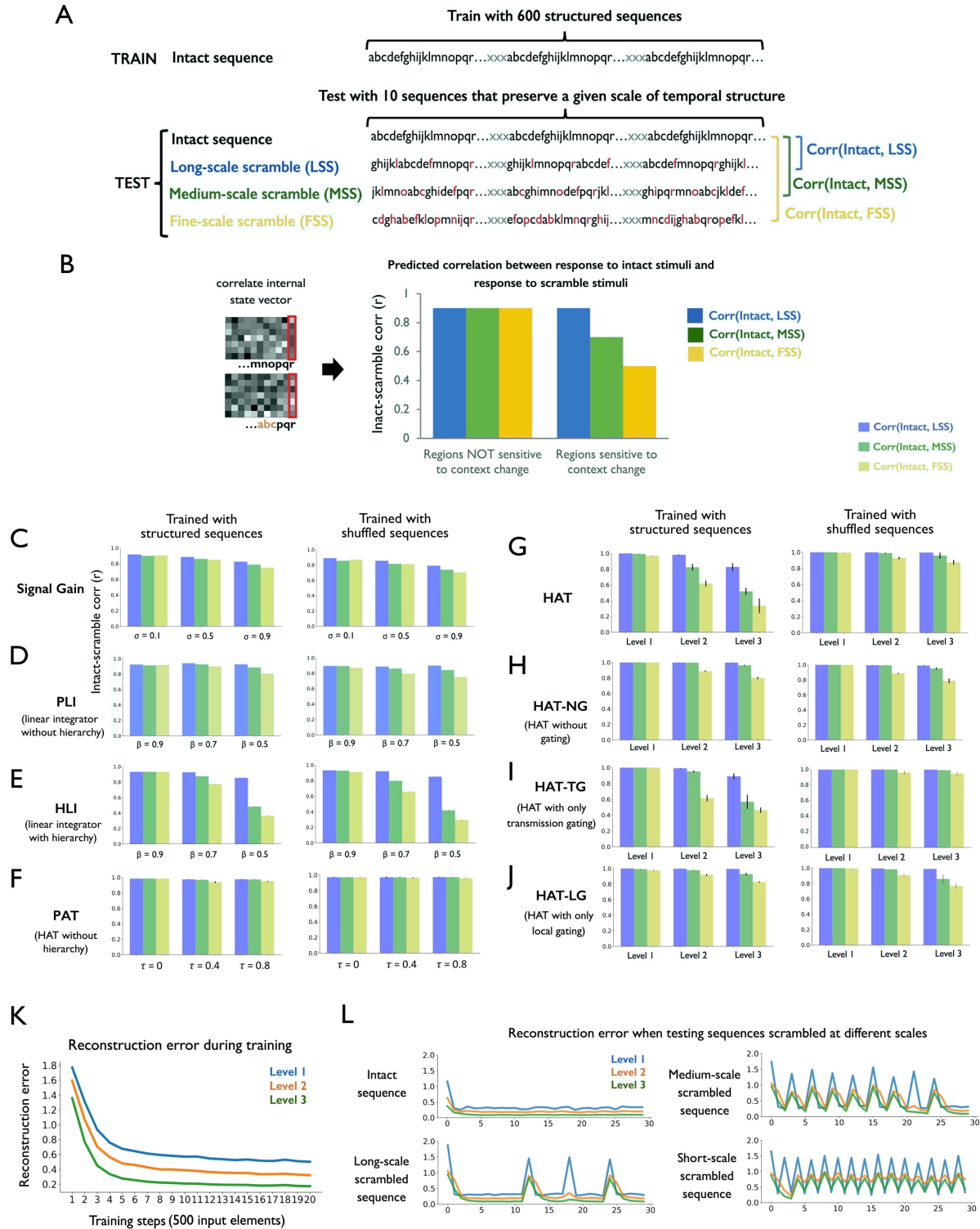


**Figure S2.** The signal gain model, linear integrator model variants and active integrator model variants account for prior data on hierarchical context dependence. Related to STAR Methods and Figures 1 and 5. (A) Example of training sequences (intact sequences) and testing sequences (long scale, medium scale and fine scale scrambled sequences). Context dependence was measured by correlating the hidden

representation between the intact and different levels of scrambled sequences. The target element (i.e. the last element of each sub-sequence) for correlation is marked with red. **(B)** The predicted correlation of hidden representations in regions that are more / less sensitive to temporal context. **(C)** The signal gain model was able to account for both of the key empirical phenomena of hierarchical context dependence (P1 and P2, above). Because the noise added to the internal representations varied in magnitude across processing stages and across levels of scrambling, the signal gain model generated the pattern of hierarchy of context dependence: the higher “stages” of the signal gain model generated lower correlation between intact and scrambled stimuli (left). We observed a similar pattern when testing the model on temporal structures that it was never trained on (right). One could plausibly amend the signal gain model to generate a learning effect, by positing that the noise level is increased when processing unfamiliar stimuli. Overall, we conclude that the signal gain model could account for the phenomenon of hierarchical context dependence. **(D)** The PLI model showed more sensitivity to context change when the  $\beta$  parameter was decreased (i.e. when the model preserved more temporal context, analogous to the higher-levels of a hierarchical model). However, this context-dependence effect was not specific to sequences that were seen during training – it was also observed when training and testing employed completely different sequences. **(E)** The HLI model showed more sensitivity to context change at higher levels. This hierarchical context dependence effect was stronger than in the PLI model. However, this context dependence was not specific to sequences that were seen during training. **(F)** The PAT model trained with structured sequences showed more sensitivity to context change when the  $\tau$  parameter was increased (i.e. when the model preserved more hidden representation, analogous to the higher-level circuit). The effect was mild and was not specific to sequences that were seen during training. **(G)** The HAT model, when trained with structured sequences, exhibited a hierarchy of context dependence across different levels of the model. Importantly, this context dependence effect in HAT was much stronger when the model was trained and tested on the same sequences. In other words, the context dependence in HAT depends on the model’s learning of temporal structure. **(H)** The HAT variant with no gating mechanism (HAT-NG) showed a similar pattern to the PLI and signal gain results: the higher levels of the model showed more context dependence, but the pattern generated was not specific to the structure of the training sequences. **(I)** The HAT variant with only transmission gating (HAT-TG), when trained with structured sequences, showed a hierarchy of context dependence across different levels of the model. This context effect was even stronger when the model was trained and tested on the same sequences. **(J)** The HAT variant with only local gating (HAT-LG) showed a hierarchy of context dependence across different levels of the model, but the pattern generated was not specific to the structure of the training sequences. **(K)** During training with the structured sequences, all levels of the HAT model exhibited a decrease in reconstruction error  $\Delta$  with increasing training duration. **(L)** Layer-specific reconstruction error in the HAT model when testing with different levels of scrambled sequences: intact sequence, long-scale scrambled sequences, medium-scale scrambled sequences and fine-scale scrambled sequences. More finely scrambled sequences generated larger reconstruction error signals. LSS = long scale scramble, MSS = medium scale scramble, FSS = fine scale scramble, PLI = parallel linear integrator, HLI = hierarchical linear integrator, PAT = parallel autoencoder-in-time, HAT = hierarchical autoencoders in time.

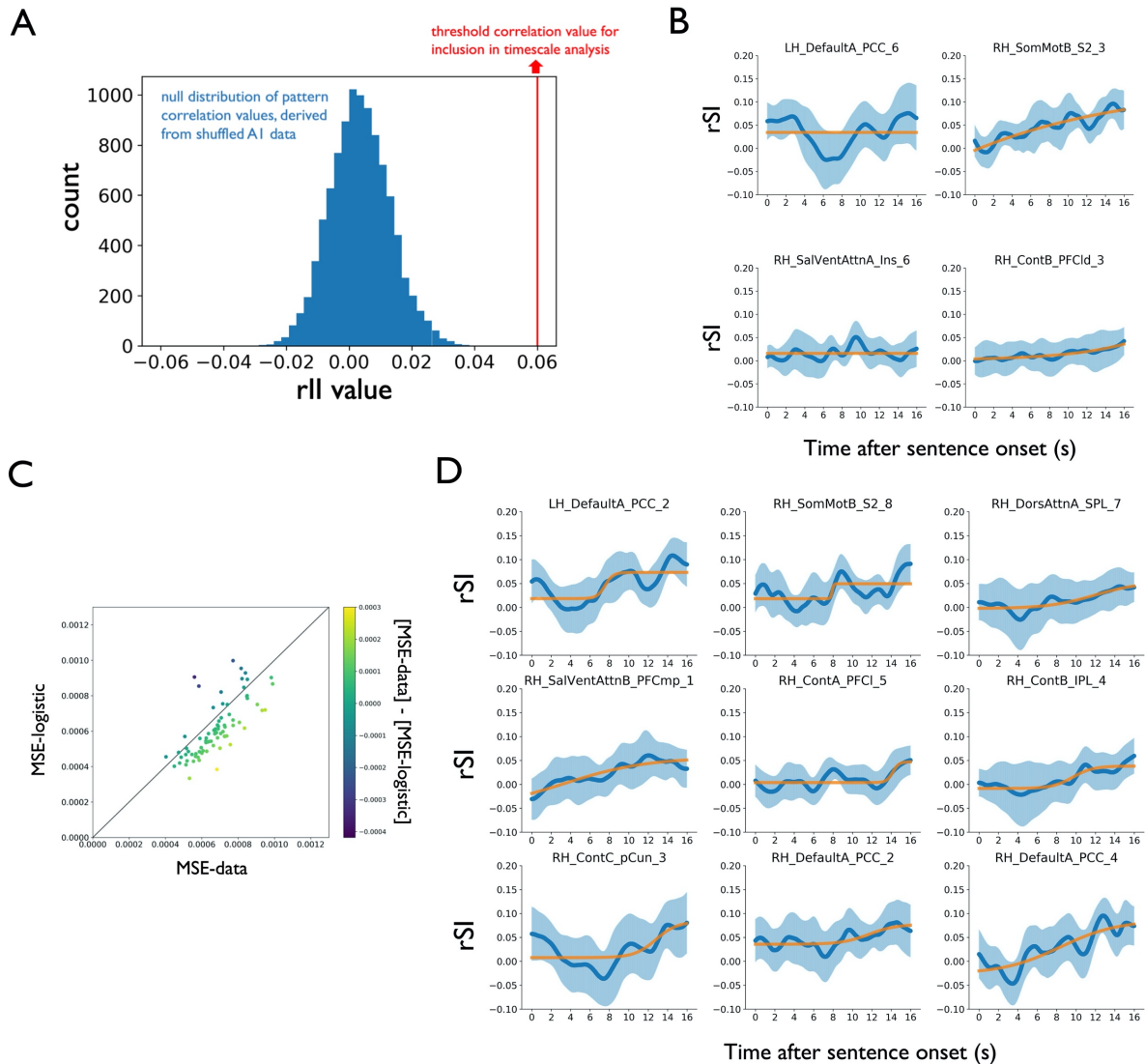
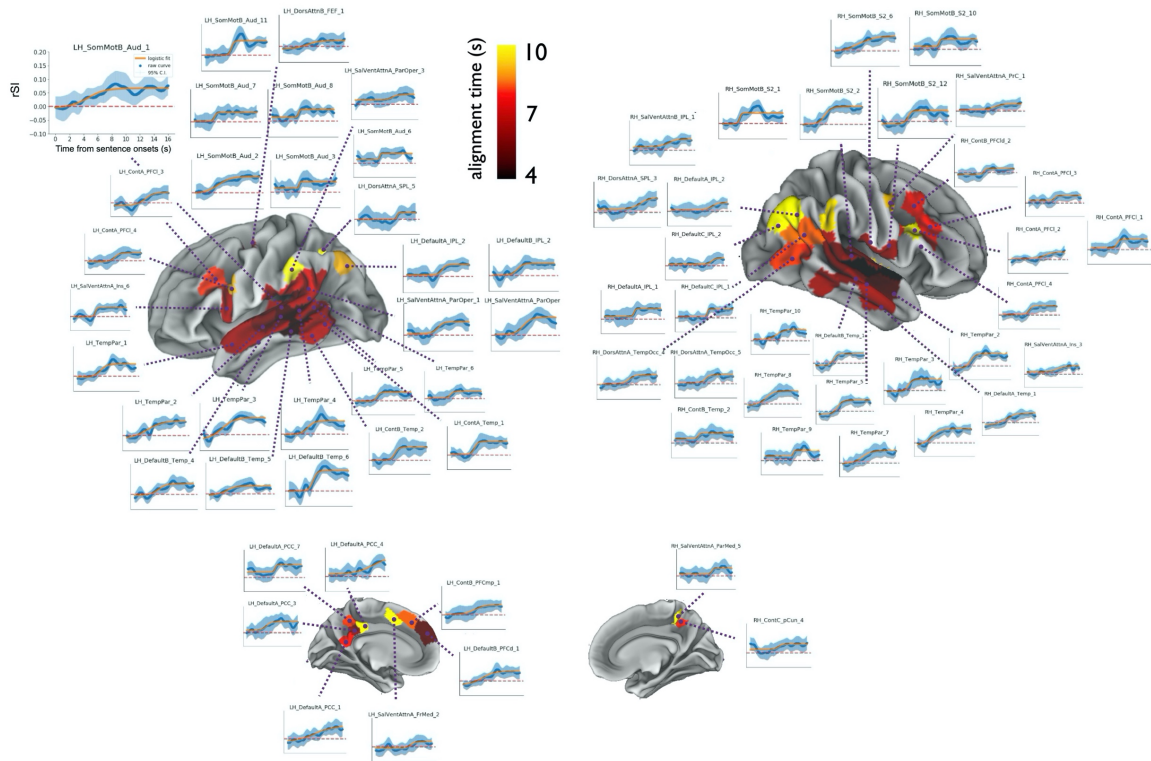


**Figure S3. Validation of ROIs for ISPC analysis and logistic model fits - raw rSI and logistic fitting curves of a set of excluded ROIs. Related to STAR Methods.** (A) The within-group ISPC (rII) was computed within an auditory cortex “A1+” parcel, which was functionally defined in a separate naturalistic narrative dataset (Simony et al., 2016). The surrogate distribution of rII values was computed by computing ISPC against non-matching sentences (shuffling the sentence order, see STAR Methods). In order to visualize the most meaningful timescale parameters in regions that responding reliably (in Figures 2 and 3), we chose a threshold of  $rII=0.06$ . This threshold was not chosen in order to correspond to an arbitrary statistical threshold, but nonetheless it is clear that  $rII= 0.06$  lies far outside the null distribution of rII values. Thus, we used 0.06 as a conservative threshold for ROIs that showed reliable stimulus-locked response. The ROIs included in Figures 2, 3 and 4 (all exhibiting  $rSS > 0.06$ ) generated a reliable stimulus-locked response to the scrambled stimulus. (B) A set of 4 anatomical regions of interest (ROIs) in which the parameters of the logistic function could not be confidently recovered after fitting the rSI curves. We visually identified parcels in which the rSI curve did not appear to follow a logistic curve. These parcels occur near left posterior cingulate cortex, right somatomotor cortex, right insula and the right prefrontal cortex. (C) The out-of-sample mean square error (MSE) in predicting rSI curves using either the raw in-sample curve or logistic model fit to the in-sample data. The error was measured using a split- half cross-validation method

(STAR Methods). For all ROIs, the MSE is similar when predicting the out-of-sample rSI curve with predictions from a logistic model and when using the raw in-sample rSI curve. For most ROIs, the error from the logistic fit is actually lower than from the raw in-sample data. This suggests that the logistic function is a valid model for the rSI curves. **(D)** A set of 9 anatomical ROIs in which the alignment time quantified by logistic fitting was not reliable across subjects. We identified these parcels by bootstrapping the logistic function parameters. The alignment time was computed for each fold of the bootstrap, from which we derived a distribution of alignment values. When more than 10% of these bootstrapped alignment time values were more than 3s different from our original alignment time estimate, we considered the ROI unreliable. The unreliable parcels occurred near bilateral posterior cingulate cortex, right precuneus, right prefrontal cortex, right superior and inferior temporal lobule, and right somatomotor cortex. The parcels are individually labeled with their names from the Schaefer parcellation (Schaefer et al., 2018). A1 = primary auditory cortex, rII = intact-intact inter-subject pattern correlation, rSS = scramble-scramble inter-subject pattern correlation, rSI = scramble-intact inter-subject pattern correlation.

**A**



**B**

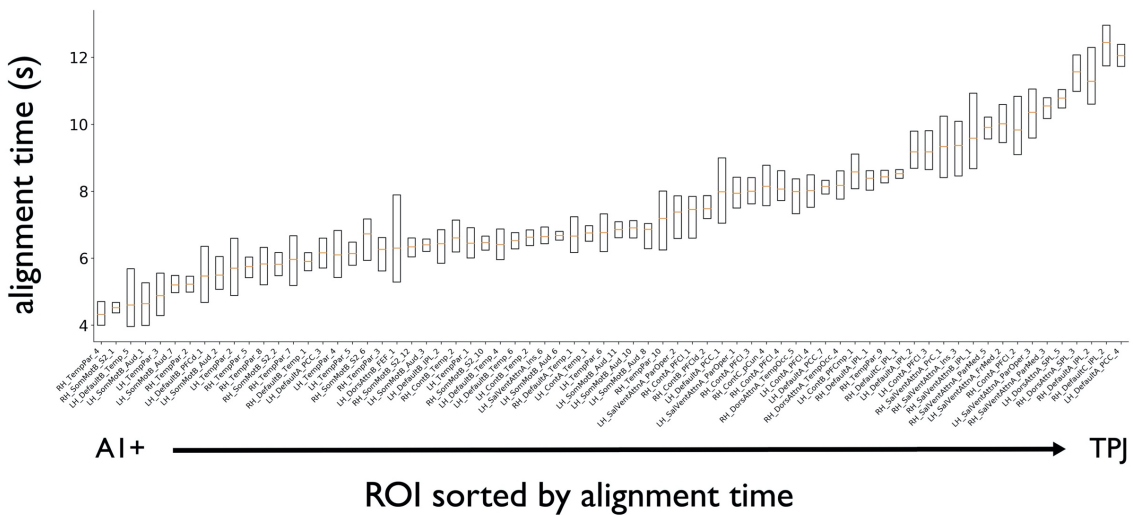


**Figure S4. The temporal profiles of context construction mapped for each ROI individually. Related to Figure 3. (A)** The raw  $rSI_{DE:CE}$  curves (blue curves) are overlaid with their corresponding logistic fits (orange lines) for each ROI. The shaded blue area indicates a parametric 95% confidence interval on each  $rSI$  measurement at each time point. Colors on the cortical map indicate the alignment time from the logistic fits. **(B)** Bootstrapped alignment time in individual ROIs. For each ROI, the orange line shows the median of 1000 bootstrapped alignment time. The upper line of the box indicates the last data point less than Q3, and the lower line indicates the last data point higher than Q1.  $rSI$  = intact-scramble inter-subject pattern correlation, ROI = region of interest, Q3 = third quartile, Q1 = first quartile.

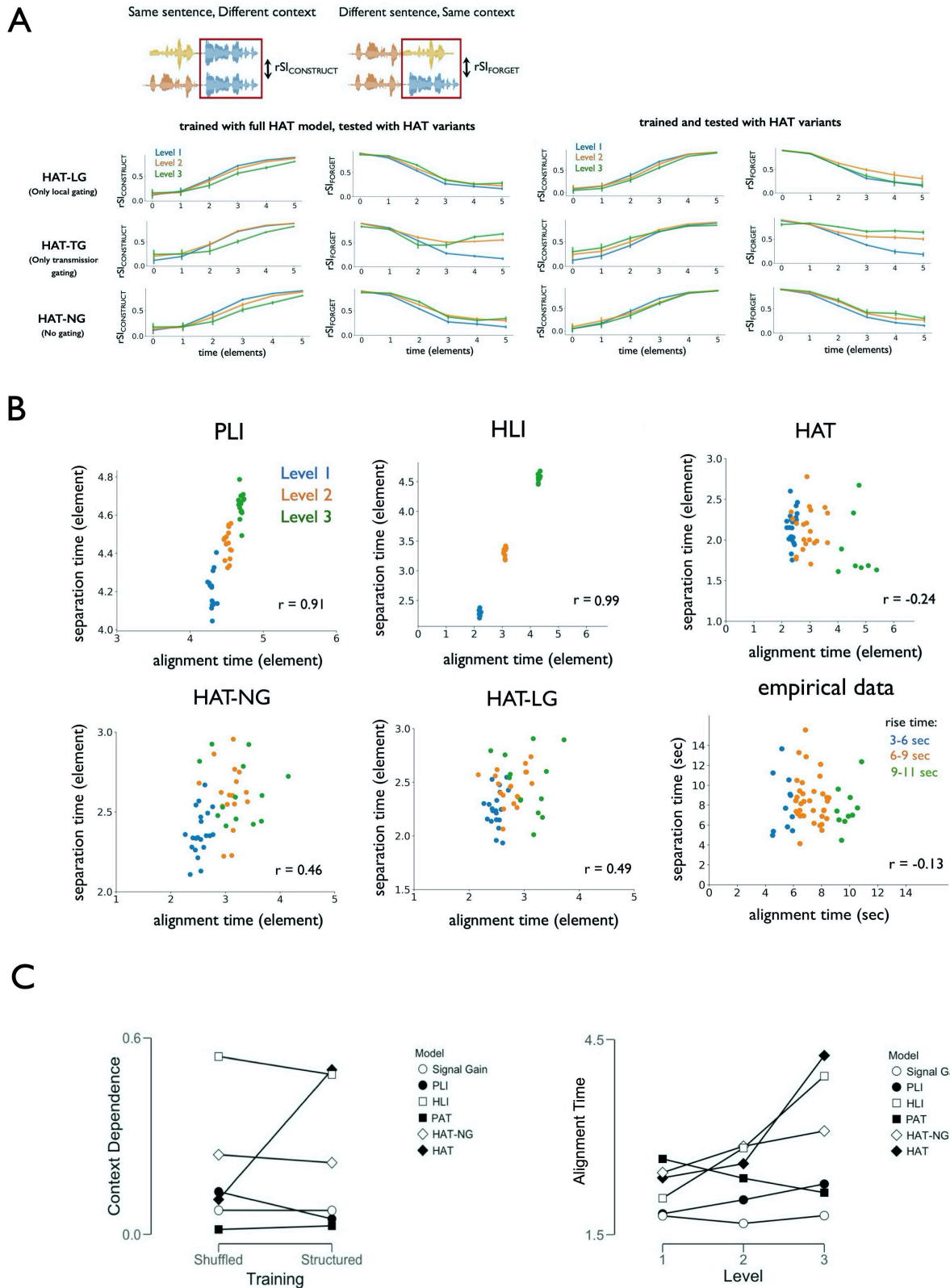
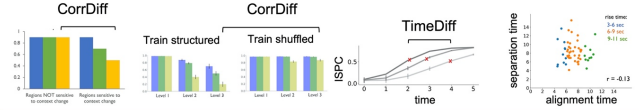


**Figure S5. Predictions of temporal integration phenomena by different computational models. Related to Figure 5. (A) Predictions of context construction ( $rSI_{CONSTRUCT}$ ) and context forgetting ( $rSI_{FORGET}$ ) for**

variants of the HAT model with limited gating mechanisms. (left) Each of these HAT variants was trained with the full HAT model (all mechanisms intact) but they were then tested with a limited gating mechanism, to evaluate the effect of gating.  $rSI_{CONSTRUCT}$  and  $rSI_{FORGET}$  generated by HAT-LG (HAT with only local gating, top), HAT-TG (HAT with only transmission gating, middle) and HAT-NG (HAT with neither local gating nor transmission gating, bottom). (right) Each of these HAT variants was both trained and tested with a limited gating mechanism:  $rSI_{CONSTRUCT}$  and  $rSI_{FORGET}$  generated by HAT-LG (top), by HAT-TG (middle) and HAT-NG (bottom). For HAT-LG and HAT-NG, the performance patterns resembled that of the linear integrator models, in which the higher levels of the model showed both longer alignment times and longer separation times. For the HAT-TG model, we found that the higher levels of the model generated somewhat nonspecific sequence representations (similar internal representations across diverse inputs). The patterns of the HAT-TG model were difficult to confidently interpret, because the separation curves were no longer logistic. Nonetheless, it appeared that HAT-TG was again similar to linear integrator models, which could reproduce the hierarchically varied alignment time for context construction, but not the distinct separation times for context forgetting. Note that higher levels of the HAT model generated more nonspecific representations when transmission gating was removed: this implies that higher levels of the model can more readily identify the beginning of a distinct new sequence when they receive “surprise” signals generated from the levels below. **(B)** Model predictions and empirical results of correlation between alignment time (time for integrating prior information) and separation time (time for forgetting prior information). PLI predicted that the alignment time is positively correlated with the separation time ( $r=0.91$ ,  $p<0.0001$ ). HLI predicted that the alignment time is positively correlated with the separation time ( $r=0.99$ ,  $p<0.0001$ ). HAT predicted that the alignment time is not correlated with the separation time ( $r=-0.24$ ,  $p=0.08$ ). HAT-NG predicted that the alignment time is positively correlated with the separation time ( $r=0.46$ ,  $p=0.0003$ ). HAT-LG predicted that the alignment time is positively correlated with the separation time ( $r=0.49$ ,  $p<0.0001$ ). The empirical results showed that for each individual ROI, the alignment time for context construction was not correlated with the separation time for context forgetting in that ROI ( $r=-0.13$ ,  $p=0.3$ ). Overall, we found that only the HAT model (which showed no correlation between alignment time and separation time) was compatible with the empirical results. Thus, within the set of models tested, context gating mechanisms are essential for capturing the empirical dissociation between alignment time and separation time. **(C)** Measurement of changes in context dependence with learning (left), and alignment time across levels (right) for a suite of models and model variants. (left) Model performance generating the phenomenon of hierarchical context dependence (Figure S2) when tested on familiar sequences (structured) or unfamiliar sequences (shuffled). (right) Model performance in reproducing the phenomenon of hierarchical context construction, which manifests as a level-by-level increase in alignment times. Only four models successfully generated the hierarchically varied alignment time, as quantified by logistic fitting – the PLI model, the HLI model, the HAT-NG model and the HAT full model. Out of the four models, the alignment time difference was much larger for HLI ( $\Delta$  Alignment Time = 1.88) and HAT model ( $\Delta$  Alignment Time = 1.88) than for the PLI model ( $\Delta$  Alignment Time = 0.46) and HAT-NG model ( $\Delta$  Alignment Time = 0.64). The signal gain model showed no difference between alignment time at Level 1 and Level 3 of the model. As noted above, the PAT model did not successfully learn distinct internal representations for different sequence items; as a result is showed larger alignment time at Level 1 than Level 3: this occurred because the ISPC values in the PAT model were higher for Level 3 than for other levels (even for random pairs of stimuli), this biased the alignment time downward, because the alignment curve ramped upward from a very high baseline value. HAT = hierarchical autoencoders in time,  $rSI$  = scramble-intact inter-subject pattern correlation, PLI = parallel linear integrator, HLI = hierarchical linear integrator, HAT-NG = HAT with no gating mechanism, PAT = parallel autoencoders in time.



Models	hierarchical architecture	nonlinear temporal integration	context gating mechanism	Hierarchical context dependence $\Delta \text{Corr}(\text{Level 1, Level 3})$	Learning effect $\Delta \text{Corr}(\text{Structured, Shuffled})$	Hierarchically varied alignment time $\Delta \text{Alignment Time}(\text{Level 1, Level 3})$	Alignment Time $\neq$ Separation Time $\text{Corr}(\text{Alignment Time, Separation Time})$
Signal Gain Model	X	X	X	0.07	0.00	0.00	N/A
Parallel Linear Integrator (PLI)	X	X	X	0.05	-0.08	0.46	0.88
Hierarchical Linear Integrator (HLI)	✓	X	X	0.49	0.05	1.88	1.00
Parallel Autoencoders in time (PAT)	X	✓	X	0.03	0.01	-0.51	N/A
HAT-no gating (HAT-NG)	✓	✓	X	0.22	0.02	0.64	0.71
Hierarchical Autoencoders in time (HAT)	✓	✓	✓	0.50	0.40	1.88	-0.24

**Table S1. Comparison of model performance across a set of four empirical phenomena: hierarchical context dependence; learning-dependent integration; hierarchical alignment times; and the decoupling of alignment time and separation time. Related to STAR Methods and Figure 5.**

Summary of model architectures and computational mechanisms (gray shading) and performance across four metrics (blue shading). Hierarchical context dependence is the basic hierarchical context phenomenon reported in prior studies and modeled in Figure S2. The learning effect is a measure of whether hierarchical context dependence is selectively observed for familiar (structured) vs unfamiliar (shuffled) sequences, as tested in Figure S2B and Figure S5C. The hierarchical variation in alignment time is a measure of the difference in alignment time between lower and upper levels of the model, intended to capture the empirical phenomenon of hierarchical context construction (Figure 3) modeled in Figure S5C. Finally, the absence of a correlation between alignment time and separation time is the phenomenon reported here (Figure 5) and modeled in Figure S5B.

To test the importance of *hierarchical architecture*, we can compare the HLI and HAT models against variants which operate with “parallel” levels. In these models (i.e. PLI and PAT), each unit receives input directly from the environment, but integrates the information with distinct time constants. These “parallel” integrator models produced smaller context effects than the equivalent models with a stage-by-stage integration process (Figure S5C). Thus, in light of the anatomical evidence for hierarchical organization, hierarchical processing appears to be an important feature for temporal processing. To test the importance of *context gating mechanism*, we tested HAT variants with reduced or absent gating mechanisms. These HAT variants generated predictions similar to the linear integrator models: they exhibited hierarchical context effects, but alignment time and forgetting time were robustly correlated ( $r = 0.46$ ,  $p = 0.0003$ , Figure S5B and Figure S5A, right). In addition, HAT variants that lacked gating learned less distinct representations of sequence elements (Figure S5A) and their integration processes were less affected by sequence familiarity (Figure S5C). Thus, a context gating mechanism appears essential for HAT-like models to capture the empirical data.

We also tested the importance of the *nonlinear temporal integration* implemented in the HAT model (i.e. the model state at time  $t+1$  is a nonlinear function of the state at  $t$  and the input at  $t$ .) A nonlinear integration mechanism is not sufficient to account for the empirical data on its own, because HAT variants without gating (but with nonlinear integration) exhibited small learning effects and their alignment times correlated with their separation times (Figure S5B, C). However, none of the linear models could account for the full pattern of data (i.e. the four metrics), and the full HAT model equipped

with the full context gating mechanism, was the most successful. Thus, within the panel of models tested, nonlinear integration improves model performance when combined with a context gating mechanism.